EXPERIMENTAL ANALYSIS *of* FIRE-INDUCED FLOWS *for the* FIRE SAFE DESIGN *of* DOUBLE-SKIN FAÇADES

STEFFEN KAHRMANN

A thesis submitted for the degree of
Doctor of Philosophy in Fire Safety Engineering

THE UNIVERSITY
of EDINBURGH

2016

To my parents

Declaration

This thesis and the work described within have been completed solely by Steffen Kahrmann at the BRE Centre for Fire Safety Engineering at the University of Edinburgh, under the supervision of Prof. José Luis Torero and Prof. Luke Bisby. Where others have contributed or other sources are quoted, references are given.

Steffen Kahrmann

July 2016

Table of Contents

Figures

Abstract

Today, ever changing and advancing techniques of construction are constantly pushing the envelope of structural possibilities in the built environment. Although not new, the concept of Double-Skin Façades (DSF) finds increasing implementation with the advent of sustainable construction, aiming to reduce energy consumption to condition buildings whilst improving indoor air quality.

As is the case with the traditional concept of the compartment fire, methodologies and assumptions on which our general understanding of the fire problem is based, did fundamentally not change. Inherently bound to this, is the concept of compartmentalisation, prescribing measures to avoid horizontal and vertical fire spread in buildings. A DSF, most commonly featuring a ventilated cavity between curtain wall and the secondary glass façade at an offset, is prone to drastically alter fire and smoke behaviour once able to enter. Unlike curtain walls, the chimney-like aspect ratio of such façades is able to trap fire and combustion gases within the cavity, potentially compromising the integrity of the building perimeter above the fire.

The current approach to this issue tends to focus on using non-combustible construction materials and the installation of sprinkler systems to avoid breakage of window panes in the first place. Another topic of interest is the weak connection between floor slab and curtain wall which can allow vertical fire spread to adjacent floors. Research has also been discussing the use of mullions to deflect the fire plume away from the façade. Even if useful in DSF's, aesthetics and problems with functionality will most likely prevent mullions from being introduced into the DSF. However, very little relevant research actually investigated the fire-induced flow structure under these conditions so that properly informed design decisions can be made.

The project at hand aims to understand hazards to the floors above and below the fire floor by experimentally investigating the governing processes by means of large-scale fire testing and small-scale salt-water modelling (SWM). The gathered data shall serve as a basis to discuss current spandrel and cavity design decisions. Results

have been compared in terms of dimensionless numbers and demonstrate complex interactions between DSF cavity width and spandrel height, encouraging a discussion about the need of further research of this topic.

Acknowledgements

First and foremost I would like to thank both of my supervisors. Prof. José Torero for offering and enabling countless experiences of a life-time throughout this journey. His exceptional way of managing people and challenges, including myself, has truly been an inestimable lesson which I am sincerely grateful for. And Prof. Luke Bisby for being an unfailing source of positivity, unmatched support and advice whenever needed and for keeping me sane in the 'Stans.

In particular I would like to thank Prof. Andre Marshall from the University of Maryland for his unconditional guidance and for allowing me to use his experimental resources at UMD. In the same breath I would like to thank Thomas Layton and Dr. Paolo Santangelo for their immense help during the salt-water modelling tests.

Special thanks go to Cecilia & Adam and Holly & Craig for too many things to mention here, but most importantly their friendship.

Thanks to the Edinburgh Fire Group (former and current) and in particular to Michal, Cristián, Adam B., Agustin, Ryan, Juan, Angus, David, Nico, Hubert, Francesco and Josephine. Those times with you all will be greatly missed.

Extended thanks go to Sebastien, Diane, Sharon, Mary Lou, Jero, Rick, Luis, Adrien, Jurij and Gerardo (from the University of Maryland and Queensland) who, in one way or another, made all this a fantastic experience.

Finally, I would like to thank Fabienne and my family, in particular my parents for their tremendous support throughout my PhD.

Nomenclature, Acronyms

Notation

A_i	Cross-sectional area of a vent [m^2]
A_W	Area of the ventilation opening [m^2]
f	Camera F-Stop number
g	Acceleration due to gravity, ~9.81 [m/s^2]
H	Height of the ventilation opening [m]
H_D	Clean layer height
H_N	Height of the neutral plane [m]
H_1	Compartment height [m]
H_2	Smoke layer height [m]
H_3	Ventilation opening height [m]
H_4	Clean layer height [m]
H_5	Compartment depth [m]
L_e	Entrance length
$\dot{m}$	Burning rate [kg/s]
n	Shape factor
P_{ext}	Atmospheric pressure [Pa]
P_{int}	Internal compartment pressure [Pa]
P_o	Pressure outside cavity [Pa]
T_a	Temperature of ambient air [kg/m^3]
T_c	Temperature inside cavity [°C]

T_g	Temperature of the hot gas layer [°C]
T_o	Temperature outside cavity [kg/m^3]
u	Velocity [m/s]
u_i	Generic characteristic velocity of fluid in any direction [m/s]
u_{in}	Velocity of inflow [m/s]
u_{out}	Velocity of outflow [m/s]
x_1	Spandrel height [mm]
x_2	Cavity width [mm]
Z^*	Height (dimensionless) ($Z^* = \frac{z}{L_2}$)
ρ_a	Density of ambient air [kg/m^3]
ρ_c	Density in cavity [kg/m^3]
ρ_g	Density of the hot gas layer [kg/m^3]
ρ_i	Generic density of fluid [kg/m^3]
ρ_o	Density outside cavity [kg/m^3]

Salt-Water Modelling Related Notion

a_1	Spill zone interrogation region
a_2	Cavity interrogation region
a_3	Injection source
a_4	Laser light sheet location
c_d	Discharge coefficient [dimensionless]
c_p	Specific heat capacity [J/K]

D	Inter-plate spacing [mm]
d_{diff}	Diffraction limited image diameter
d_i	Pixel size estimate [μm]
d_I	Width of the interrogation region (i.e. cavity width) [mm]
d_p	Seeding particle mean diameter [μm]
Gr_{source}^{fire}	Fire source based Grashof number (dimensionless)
Gr_{source}^{sw}	Salt-water source based Grashof number (dimensionless)
H	Height of the compartment opening [mm]
h_{in}	Plane height of inflow [m]
h_{out}	Plane height of outflow [m]
L_f	Characteristic length scale for salt-water for fire case
L_{sw}	Characteristic length scale for salt-water case
M	Magnification of optical system
$\dot{m}_{f,e}$	Mass flow rate of fresh water entrainment
$\dot{m}_{f,i}$	Mass flow rate of salt-water injection
$\dot{m}_{f,o}$	Mass flow rate of exiting salt-water / fresh water mixture
m_{sw}^*	Salt-water source strength parameter (dimensionless)
$\dot{m}_{in}$	Mass flow rate of spill into cavity [m^2/s]
N	Neutral plane
N_I	Particle image density
p^*	Pressure (dimensionless)
P_0	Pressure inside cavity
P_∞	Ambient pressure

Pr	Prandtl number
Q^*	Fire-induced source strength parameter (dimensionless)
$\dot{q}^*$	Fire-induced volumetric energy release rate (dimensionless)
Ra	Rayleigh number
Ra_D	Rayleigh number based on inter-plate spacing
Ra_H	Rayleigh number based on cavity height
Re	Reynolds number
Sc	Schmidt number
t^*	Time (dimensionless)
u_j^*	Velocity (dimensionless)
$\bar{u}$	Average flow velocity
$V_{c,fd}$	Characteristic velocity in fully developed flow
$V_{c,bl}$	Characteristic velocity in boundary layer flow
$\dot{w}_{sw}^*$	Salt-water volumetric energy release rate (dimensionless)
W	Width of the compartment opening
x_i^*	Position (dimensionless)
ΔX	Relative in-plane image displacement per particle
Y_{salt}	Salt mass fraction
Δz	Relative out-of-plane displacement
Δz_0	Thickness of the laser light sheet
β_T	Constant (thermal volumetric expansion coefficient)
β_{sw}	Constant (= 0.76)
θ_{sw}^*	Salt-water density difference (dimensionless)

θ_T^*	Fire-induced density difference (dimensionless)
δ_T	Boundary layer thickness
ρ_∞	Freshwater density [kg/m^3]
ρ_0	Salt-water density [kg/m^3]
ν	Kinematic viscosity [m^2/s]
λ	Wavelength of incident light [m]

Acronyms

BRE	Building Research Establishment
CCD	Charge-Coupled Device
CFD	Computational Fluid Dynamics
DG	Dimensionless Group
DNS	Direct Numerical Simulation
DSF	Double-Skin Façade
ETFT	Edinburgh Travelling Fire Tests
FDS	Fire Dynamics Simulator
FOV	Field of View
HF	Heat Flux
HFG	Heat Flux Gauge
HRR	Heat Release Rate
LES	Large Eddy Simulation
LIF	Laser Induced Fluorescence

PF	Post-Flashover
PIV	Particle Image Velocimetry
PLIF	Planar Laser Induced Fluorescence
SWM	Salt-Water Modelling
TC	Thermocouple
TSC	Thin-Skin Calorimeter
VSS	Vertical Smoke Spread

1 Introduction

1.1 Generalities of the Double-Skin Façade

Poirazis [1] states that although their concept is not new, the implementation of double-skin façades (DSF) by architects and engineers is on the rise in recent times. In Europe this is mainly driven by aesthetics asking for fully glazed facades which also shall improve the indoor environment for occupants living and working in these spaces. But also reduction of noise levels from ambient and energy consumption are reasons for this trend. Previous research mostly focussed on general architecture, better utilization of perimeter area, improvement of the environmental footprint of the building and energy use. The concept of DSFs is complex and its parameters often interact with each other.

The general structure of a DSF system is described by the Belgian Building Research Institute [2] as follows (for details see Figure 1-1):

- Exterior Glazing: Usually hardened single glazing. Which can be fully glazed
- Interior glazing: Units of insulating double glazing (clear, low E coating, solar control glazing, etc.). Almost always this layer is not fully glazed.
- Air cavity (between int. & ext. panes): Can be natural, fan supported or mechanically ventilated. The width of the cavity can vary depending on the applied concept between 0.2 m to more than 2.0 m.
- Interior openings: If existent, are user operable which allows for natural ventilation to the interior.
- Shading devices: If existent, are integrated inside the air cavity.

Additional details e.g. are metal grates on horizontal supports inside the cavity. These walkways on floor level can be used as emergency escapes and for cleaning and servicing of the system.

Loncour et al [3] identify three main criteria to classify DSFs which are the type of ventilation, the partitioning of the façade and the ventilation modes of the cavity.

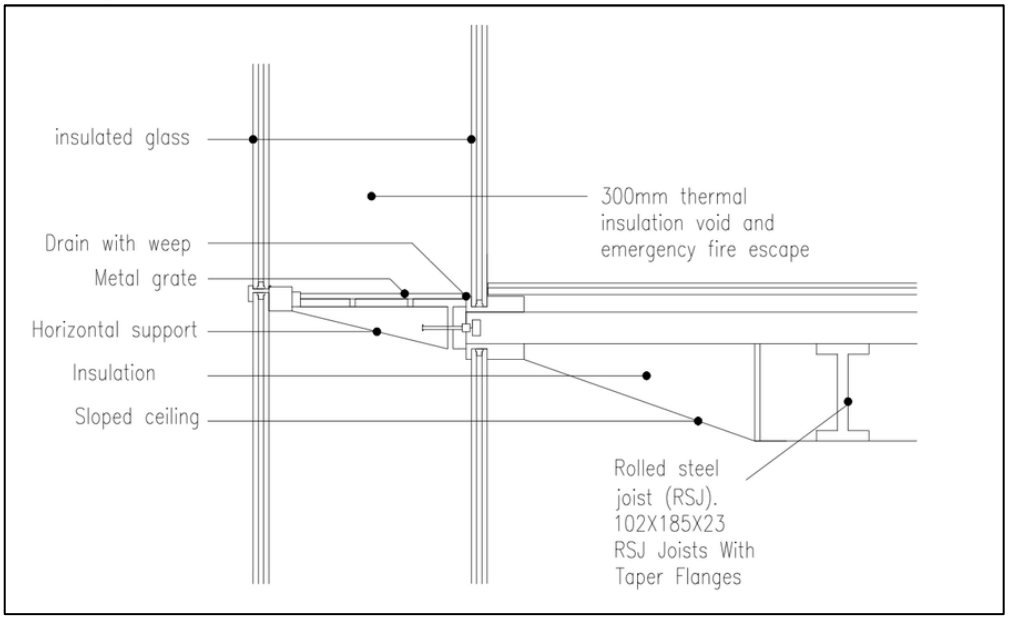

Figure 1-1 Construction detail of a Double-Skin Façade (example, dimensions vary) [4].

1.1.1 Type of Ventilation

The driving forces between the two faces of a DSF can basically be categorized in three separate modes (natural-, mechanical- & hybrid ventilation). Natural ventilation, not assisted by powered air movement, utilizes pressure differences created by the stack effect and wind effects. In contrast, mechanical ventilation relies on powered equipment to move air. The hybrid system is basically a naturally ventilated façade where a control system switches to mechanical ventilation in cases where circumstances are no longer sufficient to ensure natural ventilation.

Partitioning of the Façade:

DSFs are distinguished by their partitioning, physically dividing the cavity between the two faces. Most commonly these types are:

- partitioned by storey
  - box-window (juxtaposed single modules)
  - corridor type
- shaft-box type
- multi-storey type
- multi-storey louver type

Box-Window Façade:

In this setup the façade is constructed of separate isolated double-skin glass pane modules, horizontally delimited by the width of the modules themselves, vertically by the height of each storey (Figure 1-2 (a)).

Corridor-Façade:

A corridor type façade is also partitioned by storey but mostly not delimited horizontally. It generally extends across several offices or entire floors and is accessible by walkways (Figure 1-2 (c)).

Shaft-Box Façade:

Compared to storey-partitioned façades, the objective of this concept is to increase the stack effect and hence enhance natural ventilation and thus, can only be applied to naturally ventilated facades (Figure 1-2 (b)).

The façade is constructed of a combination of box-window façade and vertical, multi-storey ventilation ducts in which the box windows exhaust indoor air. The air flow of the duct evacuates at an outlet several floor above.

Multi-Storey Façade:

This type of façade is not partitioned horizontally or vertically, creating one large volume between inner and outer façade. In some cases, this volume wraps around the entire building. For ease of accessibility, most multi-storey facades feature walkways at each floor level and are predominantly naturally ventilated. For heavily noise polluted areas, this type of façade promises the highest reduction of indoor noise levels (Figure 1-2 (d)).

Multi-Storey louvered Façade:

Fundamentally the same concept as the multi-storey façade, this type features an operable outer façade with pivoting louvers. It has to be noted that, even when fully closed, the outer face is not completely airtight.

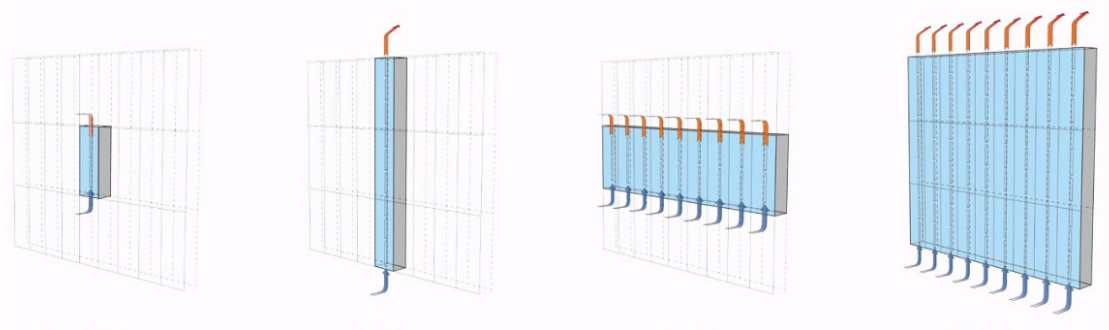

Figure 1-2 Overview of DSF concepts (a-d, left to right), box-window façade, shaft-box façade, corridor-façade, multi-storey façade [5].

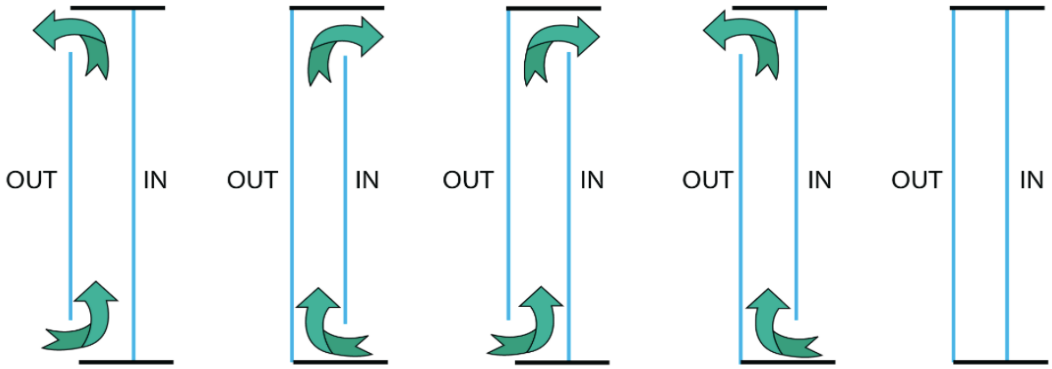

Figure 1-3 Overview of DSF ventilation types (left to right), outdoor air curtain, indoor air curtain, air supply, air exhaust, buffer zone [5].

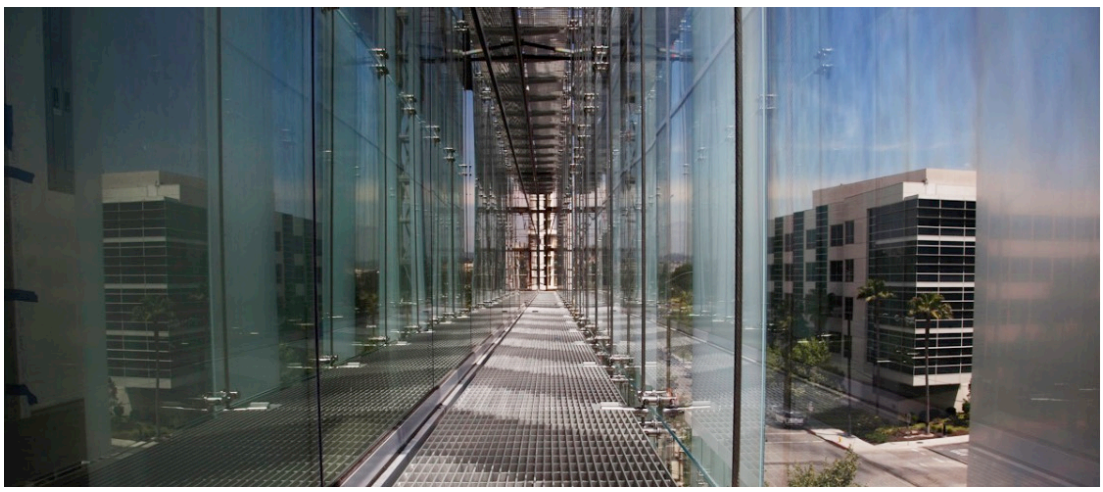

Figure 1-4 View inside a multi-storey DSF [5].

1.1.2 Ventilation Modes

The ventilation mode, independent and not to be confused with the ventilation type, refers to the flow path of the circulating air through the cavity. Depending on the type of façade, several ventilation modes can be achieved but not all facades are able to adopt all of the modes.

In general, a distinction is made between five main ventilation modes:

- Outdoor Air Curtain: Air enters the cavity space from the outside and gets expelled to the outside.
- Indoor Air Curtain: Indoor air enters the cavity and exhausts into the inside.
- Air Supply: The façade supplies the indoor environment with outdoor air via the façade cavity.
- Air Exhaust: Indoor air exhausts via the cavity to the outside.

Buffer Zone: No air flow exchanges via the façade and a buffer is created.

1.2 Smoke Migration

Double-Skin Façades usually being constructed of an inner curtain wall with an additional outer glass layer pose a specific threat in terms of vertical smoke spread (VSS; respectively fire spread) across inter-floor fire compartmentalisation. There are two main mechanisms by which VSS possibly happens in DSFs (Figure 1-5 (a)):

- Exterior Perimeter: Failure of fire proofing materials installed between floor slab edge and curtain wall occurs due to fire stops often not being mounted properly leading to failure by human error. Fire-induced warping and deflection of entire sections of the curtain wall can lead to the formation of gaps between floor slab and curtain wall which allows for VSS.

- Cavity Interior: Failure of the inner curtain wall (e.g. glass breakage due to fire) allows smoke to enter the DSF cavity space, possibly allowing for smoke / fire spread to upper floors. Unlike in usual curtain wall setups, hot combustion gases do not exhaust into ambient but are being trapped inside

the cavity void possibly having negative effects on adjacent floors of the building.

According to *Aksamija et al* [6] examples of fires with non-existent exterior perimeter fire barrier systems (EPFBS) are the First Interstate Bank Building and the One Meridian Plaza fire. In the former, the fire originated in an open-plan office on the 12th floor and spread to the 16th floor, mainly through the outer wall of the building. Curtain wall, spandrel panels and mullions where almost completely destroyed in the fire and illustrates that vertical fire spread can be rapid if no sufficient compartmentalisation is in place. In the latter case of the One Meridian Plaza building, the fire extended from the 22nd to the 30th floor through the outer walls.

Statistics by *Cowlard et al* [7] show a 2010 fire in a Shanghai residential building (28 storeys engulfed, killing 58) and the 2009 CCTV Tower fire as examples of the most severe cases of external fire spread via the curtain wall. The building's 44 floors where engulfed in fire in just 15 minutes. Both upward and downward vertical fire spread was enabled by failing compartmentalisation which historically was an extension of the floor slab past the external façade inhibiting external fire spread.

(a) (b)

Figure 1-5 Mechanisms of vertical fire spread in curtain walls (a) [8], smoke spread in a DSF fire test [9].

(a) (b)

Figure 1-6 Examples of rapid exterior fire spread. Shanghai residential building fire (a), CCTV Tower Fire (b).

With the advent of changes in building technologies (architectural, sustainability and economic reasons) the curtain wall has introduced flammable materials into the façade system posing challenges in terms of compartmentalisation which the construction industry has not fully accounted for. Also, the evaluation of fire resistance testing has not evolved accordingly since the late 1970's and standardised methods do not take fire-induced deformations of the cladding system into account [7]. Deflections, possibly leading to the formation of gaps between floor slab and curtain wall, can open pathways for vertical fire spread.

Fire Incidents in multi-storey DSFs have not been reported yet. Being an alteration of the curtain wall, it is the opinion of the author, that these will inevitably occur more often in the future due to the increasing number of such systems being applied in high-rise construction.

1.3 Status Quo of DSF Fire Safety

The current knowledge and research efforts in DSF fire safety are presented in this section. Additionally, respective code compliance requirements will be summarized.

1.3.1 Research Efforts and Current Knowledge

One of the first to investigate fire dynamics in DSF fires was *W.K. Chow et al* [10] in 2004. A total of 10 tests were carried out collecting temperature and heat flux data on

the inner and outer face of a DSF fire test rig which was attached to a fire compartment providing the heat source. The cavity dimensions were 2.0 m (cavity width) x 4.2 m (height) and 2.0 m (depth) and the fire source is described as a circular pan of a 0.5 m diameter filled with gasoline (test dependent 1000, 2000, 3000 & 5000 ml).

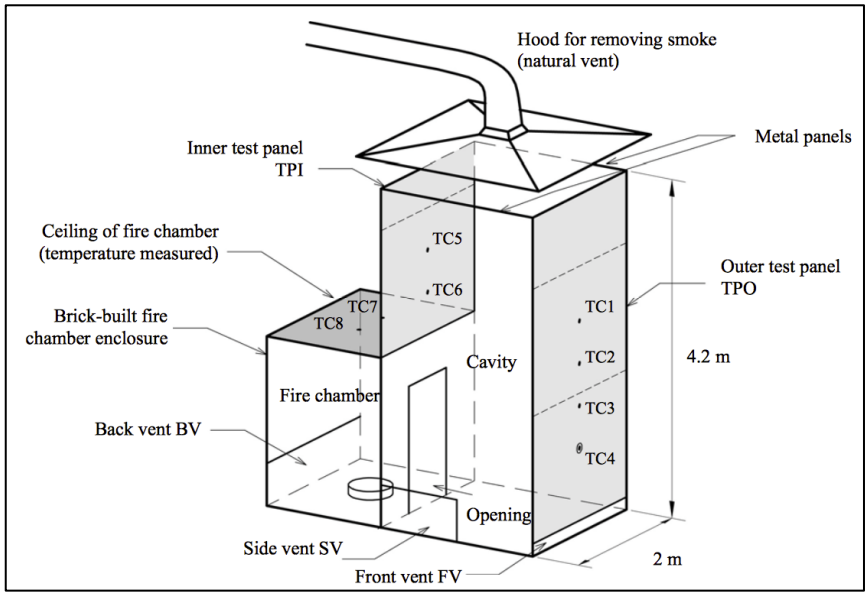

Figure 1-7 Preliminary DSF Experiment [10].

One of the aims of this study was to characterise the fire-induced flow establishing between the inner- and outer DSF face at a constant cavity width of 2.0 m and a variety of heat sources and heat release rates (HRR).

The author recognises the ratio between cavity width and –height as:

> "*may be too large*", the author suggests a cavity width of 2.0 m "*might be a safe value for this new feature [i.e. DSF]. Undesirable fire scenarios might be caused by a value less than that.*" The author further states that generally "*hot gases moved towards the outer skin of the double-skinned façade*" and that "*temperature at [vertical locations along outer skin] decreased with [decreasing] height*."

Although the author of the thesis at hand disagrees with the experimental setup chosen and questions its ability to simulate DSF dimensions and characteristics, this preliminary study provides useful information and represents a first, necessary step

in DSF large-scale testing. It has to be noted that hot gas exhaustion was achieved by a non-mechanical smoke hood installed immediately after the cavity top opening, prohibiting a free cavity flow to establish. Also, the lateral sides of the rig where closed and supply airflow was provided through a 0.15 m gap at floor level.

Based upon the same test rig, additional conclusions are being presented by *W.K. Chow & Hung* [11] in 2006, further exploring effects of cavity width on the fire-induced flow within a DSF. Various cavity spacing of 0.5 / 1.0 / 1.5 and 2.0 m where studied. The authors state:

> "*Wider cavities might be safer in the [presented] tests. To avoid breaking of the inner glass panels, […] larger cavity space might be a solution. [...]. Cavity depth of 1 m appeared to be a more dangerous design.*" The authors further summarise "*test panel [inner face] would be eventually heated up to higher temperature for wider cavities. [Outer face] would be hotter when the cavity is too narrow. When the cavity depth is smaller, smoke spreading out from the fire chamber would impinge on the outer panel.*"

Junmei et al [12] studied the effects of cavity width on smoke spread in DSFs numerically. No description of the numerical model is given but stated it is based on the physical model presented in [10] using the same cavity widths of 0.5 / 1.0 / 1.5 & 2.0 m.

The authors state:

> "*By examining the results for cavity depth of 0.5, 1.0 and 1.5 m, it is found that a deeper cavity might give better safety under the scenarios studied. The outer glass panel would be broken rapidly for the cavity of 0.5 m deep. Cavity depth of 1 m might be the most risky design comparing the other two different cavity depths studied. The inner glass panel might be broken before the outer panel, might lead to the fire spread to the adjacent upper levels, this would give an undesirable outcome.*"

The first full-scale analysis was conducted by *Zhaopeng et al* [9] who constructed a two-storey outdoor test facility to simulate fire spill into a DSF (12.0 m length, 6.0 m height and 0.86 m cavity width). It has to be noted that the glass façade space was closed off at the bottom (sitting on ground), only allowing to draw fresh air from the sides of the void (Figure 1-5 (b)). Fire compartment dimensions were 4.0 (l) x 9.0 (w) x 3.3 (h) m. Heat Release Rates where chosen to be 1.0 MW for tests featuring an intact inner skin on the upper floor, and 2.0 MW for a test which lacked inner skin panels on this floor in order to simulate post-failure conditions of the inner façade face.

Figure 1-8 Large-scale experimental setup of a DSF [9].

The authors state:

> *"For a fire with larger HRRs [2.0 MW], the smoke could enter the cavity with a projectile horizontal velocity, hit the external façade and move upwards adhering to the external skin, resulting higher temperatures on the external skin than those on the internal skin."* and *"The breakage of the external skin would then direct the hot smoke to the atmosphere and help to decrease the high temperature and pressure in the cavity."*

As a measure to protect adjacent upper levels from fire spread through a DSF, *C.L. Chow et al* [13] proposed an apron design as described by *Zukoski* [14]. Through CFD modelling and experimental studies, horizontal spandrels/aprons are described to redirect flame impingement towards the exterior façade which then increases the

probability of its structural failure, leading to flame- and hot gas exhaustion into ambient. The interior glass panes and window frames on adjacent upper floors would then be less affected by the heat impact.

The authors further state about DSF fire dynamics:

> *"Movement of hot gases depends on the façade cavity, which is the distance of the exterior glass pane away from the interior glass pane. A vertical channel hot gas flow in a DSF with narrow cavity depth would heat up both glass panes. However, the interior glass pane and the window frame would be heated up in a fire because of differences in air entrainment below and above the flame jet. This scenario is very hazardous and should be considered in fire hazard assessment."*

Based upon the test rig already used in [10]*, C.L. Chow* presents outcomes from eight full-scale DSF fire tests [15]. Using a 6.0 m tall test rig, fire-induced flows through cavity widths of 0.5, 1.0, 1.5 and 2.0 m where investigated. Each cavity has been tested twice using a 1.2 MW fire which shall represent post-flashover (PF) fire conditions. The lateral sides of the rig where closed and supply airflow was provided through 0.15 m gaps at floor level. A fan at unsteady flow rates of 3800 to 5000 m^3 h^{-1} was used to "drive out" the fire flow into the cavity space. Without supplying further information, the author states that *"different operating schemes of the fan were adjusted for all eight tests […]."* Temperature measurements are presented in (Figure 1-9).

Three "flame spread stages" are suggested: acting at exterior pane, adhering to the upper interior pane and detaching from the exterior pane. A cavity width of 0.5 m is described as the most severe case with temperatures along the exterior pane generally higher than along the interior. A width of 1.0 m is also described to be a fire hazard to the interior face. Apparently, less problematic are cases of 1.5 and 2.0 m. A comparison of the ejected plume from the fire compartment suggests increased spread rates for DSF in contrast to single-skin facades.

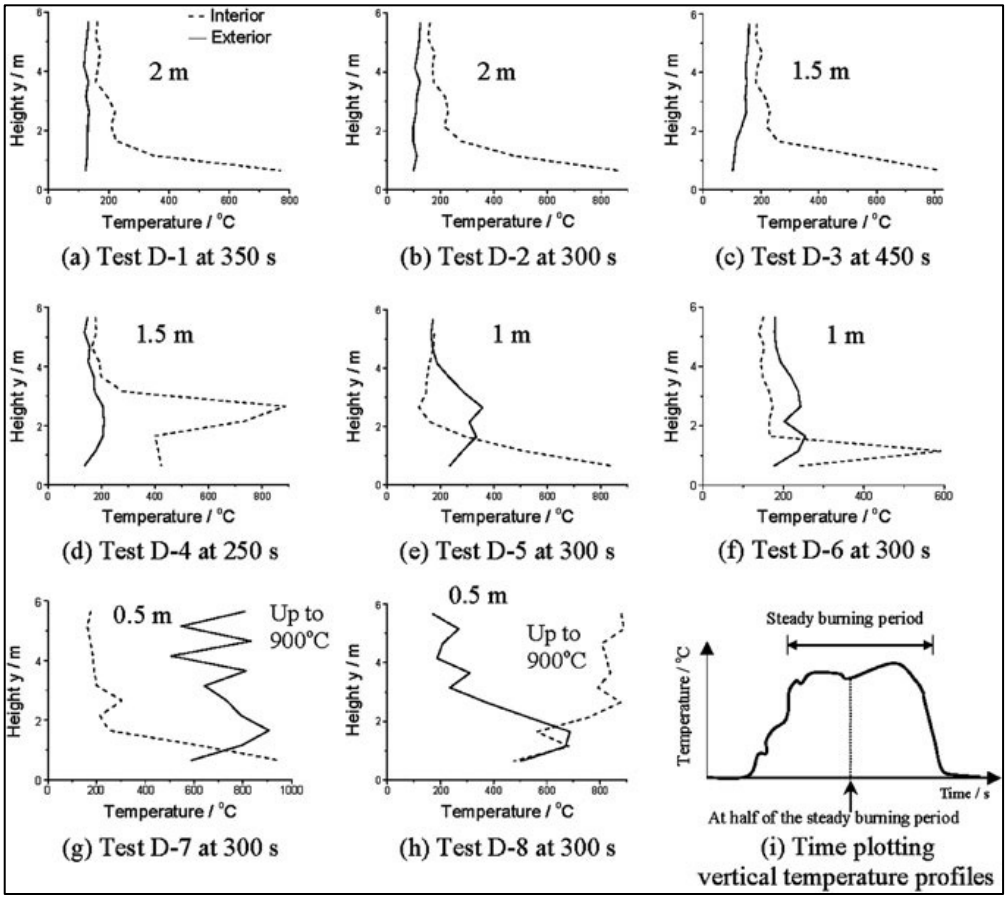

Figure 1-9 Interior and exterior temperature profiles of the fire-induced flow at various DSF spacing (eleven Thermocouples equally distributed every 0.5 m over the entire shaft height) [15].

1.4 Preliminary Observations and Summary

A general description of DSF technicalities and principles of the different flow regimes has been presented in this chapter. Vertical smoke spread via this building feature is presented chiefly in terms of the multi-storey DSF which can be said to be the worst case scenario and hence will further be studied in the thesis at hand. A summary of relevant research is given which highlights the current lack of understanding of the problem and the need for future studies to fill the knowledge gaps. One attempt to this will be the small- and large-scale experiments presented in this project, focussing on the details of the establishing cavity flow using quantitative performance metrics.

2 External Fire Flow Regimes

External fire-induced flow along a façade is chiefly influenced by internal compartment combustion processes and conditions. Interactions and linkages will be presented here in physical terms and the characteristics of the three main façade boundary layer flows (attached, reattaching and line plume) given.

2.1 The Compartment Fire

Drysdale [16] describes the term 'compartment fire' as a fire which is confined within a room or similar enclosure in a building and is of "common", room-like volumes in the order of 100 m^3. Fires in large spaces (>1000 m^3), elongated chambers and rooms of certain geometries can drastically change its behaviour.

Upon ignition and in the early stages of the fire, pyrolysis rate and energy release rate are unaffected by the compartment boundaries but solely depend on the burning of the fuel itself. If sufficient ventilation is ensured and the fire allowed to spread, fire growth continues and the confinement begins to influence the development. It can then be described in form of the HRR as a function of time.

The resulting curve features three characteristic stages:

- Pre-Flashover: low average compartment temperature, fire localised to origin.
- Post-Flashover: all combustible items involved, flames appear to fill entire compartment.
- Decay Period: begins after average room temperature has fallen to 80 % of peak value.

  Since the post-flashover stage is usually where window breakage and external flaming occurs, this study will focus on this fully developed period of a fire [16].

2.1.1 Post-Flashover Compartment Fire

After flashover occurred, all exposed surfaces of the combustible items within the room burn and the HRR develops its maximum. Typical temperatures reach 900 – 1100 °C and under certain conditions far above. This fully developed stage will

continue until the production of flammable gases begins to slow down and depicts the phase where structural damage to buildings usually occurs. Here, building elements become heated to temperatures at which they are no longer able to fulfil their function (e.g. carry design load). Depending on the structure this can cause localised or more general collapse. If compartment walls fail, fire spread is permitted to adjacent spaces by via transmission of heat or direct flame penetration [16].

In the case of DSFs, glass elements of the inner skin are prone to fail in the PF stage opening a pathway for fire and smoke spilling into the cavity space. Hence, this phase will be discussed from here on and experimental work within this thesis has been designed to reflect these circumstances by a missing inner cavity pane on the fire floor itself. The processes involved leading to glass breakage is a separate important topic to investigate but not within the scope of this work.

2.1.2 Compartment Fire Dynamics

In order to describe and understand external flow (flaming) within the DSF cavity, a brief, simplified recapitulation of internal compartment fire dynamics in the PF stage is presented here.

Drysdale [16] mentions initial work to study fully developed compartment fire behaviour was undertaken by *Kawagoe et al* [17] who measured the burning rate of wood cribs in rooms with different sizes of ventilations openings. Full- and reduced-scale tests found the burning rate ($\dot{m}$) to depend strongly on the size and shape of the ventilation opening in the form of the relationship

$$\dot{m} = 0.09 A_W H^{1/2} \; [kg/s] \qquad \textbf{Equation 2-1}$$

where

A_W = area of ventilation opening [m^2]

H = height of the ventilation opening [m]

The numerical constant however seems to a certain extent ill-defined and it is found, that the correlation only holds true over a limited range of values of $A_W H^{1/2}$ [18] [19]. The widely known interpretation is that within this range the rate of burning is

controlled by the airflow rate able to enter the compartment (ventilation-controlled). If the ventilation opening is enlarged however, the rate of burning becomes independent of the size of opening and instead is governed by the burning characteristics and surface area of the fuel (fuel-controlled). Drysdale [16] further notes that formal distinction between the two regimes has been made by [20] [21], referring to them as *Regime I* (ventilation-controlled) and *Regime II* (fuel-controlled).

Any attempt to model compartment fire flows requires a certain level of simplification to overcome the inherent complexity of the processes involved. In fire modelling, the most commonly used physically based model is the zone model which essentially solves the conservation equations for distinct and relatively large control volumes (enclosures). Zone models based on the two-layer assumption divide the fire compartment into two, stacked layers (Figure 2-1). The upper layer of hot gases contains combustion products and it is assumed, that the entire layer is at uniform temperature and density (T_g, ρ_g). The lower layer of cold gases is filled with entrainment air from ambient and is also at uniform temperature and density (T_a, ρ_a) [22].

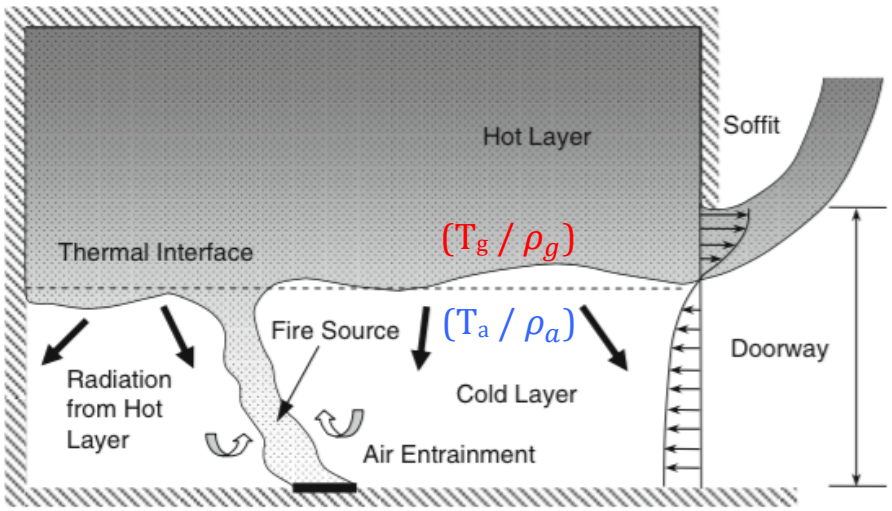

Figure 2-1 Schematic of the zone model approach [22].

2.1.3 Two-Layer Zone Model of Internal Compartment Flow

As *Majdalani* [23] recapitulates, *Kawagoe* [17] was the first to introduce a model of the compartment fire fluid mechanics. It was assumed, that the temperature

distribution within the fire compartment was uniform and entrainment air inflow and hot gas outflow via the ventilation opening was introduced by a static pressure field created by temperature and density differences between inner and outer atmosphere. Pressure and velocity profiles at the opening plane were based on the principle of energy conservation in moving fluids by means of the Bernoulli Equation.

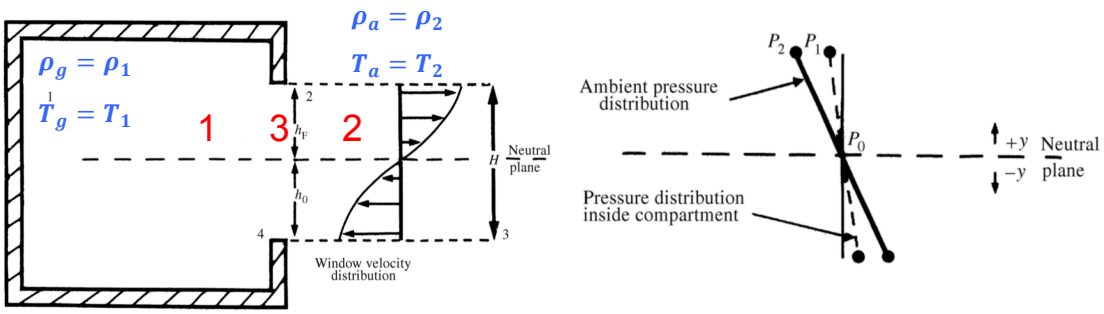

Figure 2-2 Simplified compartment fire zone model (modified from [16])

Abbreviations:

$\boldsymbol{H_3} = \boldsymbol{H} = \boldsymbol{h_f} + \boldsymbol{h_0}$ = Ventilation Opening Height

$\boldsymbol{H_N} = \boldsymbol{N}$ = Neutral Plane

$\boldsymbol{P_{ext}} = \boldsymbol{P_2}$ = Atmospheric Pressure

$\boldsymbol{P_{int}} = \boldsymbol{P_1}$ = Internal Compartment Pressure

$\boldsymbol{T_g} = \boldsymbol{T_1}$ = Internal Compartment Temperature

$\boldsymbol{T_a} = \boldsymbol{T_2}$ = External Ambient Temperature

$\boldsymbol{\rho_g} = \boldsymbol{\rho_1}$ = Internal Compartment Density

$\boldsymbol{\rho_a} = \boldsymbol{\rho_2}$ = External Ambient Density

General expressions are illustrated in Figure 2-2, where the compartment interior (1) is filled with stagnant hot gases at uniform temperature T_g and density ρ_g. Likewise the exterior, ambient atmosphere (2) is also at a (lower) temperature T_a, and thus increased density ρ_a. Both atmospheres are connected in location (3). As a need to replace the exhausting hot gas layer through the upper part of the opening, colder entrainment air flows in via the lower section of the vent.

Applying Bernoulli at any given height in (1) and (2) leads to the following description [23] (no velocity in either (1) & (2)) [23]:

$$P_1 + \rho_1 g h_1 = P_2 + \rho_2 g h_2 \qquad \textbf{Equation 2-2}$$

Considering $h_1 = h_2$, the expression for the hydrostatic pressure difference between the (1) and (2) is:

$$\Delta P_{hydrost.} = P_1 - P_2 = g(\rho_2 - \rho_1)h = g(\rho_a - \rho_g)h \qquad \textbf{Equation 2-3}$$

As for the hydrodynamic pressure difference, applying Bernoulli at a certain height between (1) and (2) and at a point in the ventilation opening between both (3) leads to the following expression (no velocity in (1-3)):

$$P_1 + \rho_1 g h_1 = P_3 + \frac{1}{2} u_3^2 \rho_3 + \rho_3 g h_3 \qquad \textbf{Equation 2-4}$$

Accounting for $h_1 = h_3$ and $\rho_1 = \rho_3$, the final equation for $\Delta P_{hydrost.}$ at a height above the neutral plane between (1) and (2) is:

$$\Delta P_{hydrost.} = P_1 - P_3 = \frac{1}{2} u_3^2 \rho_3 = \frac{1}{2} u_{out}^2 \rho_g \qquad \textbf{Equation 2-5}$$

When in motion, the hydrostatic pressure is completely converted into hydrodynamic pressure. Thus:

$$\Delta P_{hydrost.} = \Delta P_{hydrodyn.} \qquad \textbf{Equation 2-6}$$

Ventilation flows in heated compartments where almost stagnant volumes of hot and cold air intersect at the opening plane, are the underlying physical concept which

defines the ventilation mode in a compartment fire. Combining the expressions for hydrostatic and hydrodynamic pressure differences and

$$\Delta P_{hydrost.} = \Delta P_{hydrodyn.}$$ **Equation 2-6**

leads to:

$$g(\rho_a - \rho_g)h_i = \frac{1}{2}u_{out}^2 \rho_g$$ **Equation 2-7**

The velocity of the exhausting hot gases at a given height h_i (above the neutral plane), can be found by:

$$u_{out} = \sqrt{2g\left(\frac{\rho_a - \rho_g}{\rho_g}\right)h_i}$$ **Equation 2-8**

According to [23], *Kawagoe* [17] introduced an expression of the velocity through an orifice based on the hydrostatic pressure:

$$u_i = \sqrt{\frac{2\Delta P_{hydrostat.}}{\rho_i}}$$ **Equation 2-9**

Further findings by [21] allowed for expressions of volumetric and mass flow rates:

$$\dot{V}_i = c_d A_i u_i = c_d A_i \sqrt{\frac{\Delta P_{hydrostat.}}{\rho_i}}$$ **Equation 2-10**

$$\dot{m}_i = \rho_i \dot{V}_i = \rho_i c_d A_i \sqrt{\frac{\Delta P_{hydrostat.}}{\rho_i}} = c_d A_i \sqrt{2\Delta P_{hydrostat.} \rho_i}$$ **Equation 2-11**

Where c_d is an appropriate dimensionless discharge coefficient for the opening and A_i the cross-sectional area of the vent [m^2] [23].

Further improvements to the flow model have been made by *Prahl & Emmons* [24] who added a uniform cold layer beneath the (uniform) hot gas layer at ceiling height (Figure 2-3). Although further adapted for the other phases of a compartment fire, this version of the flow model is still in use today. Smoke layer build-up is enabled by the size and position of the vent opening [23].

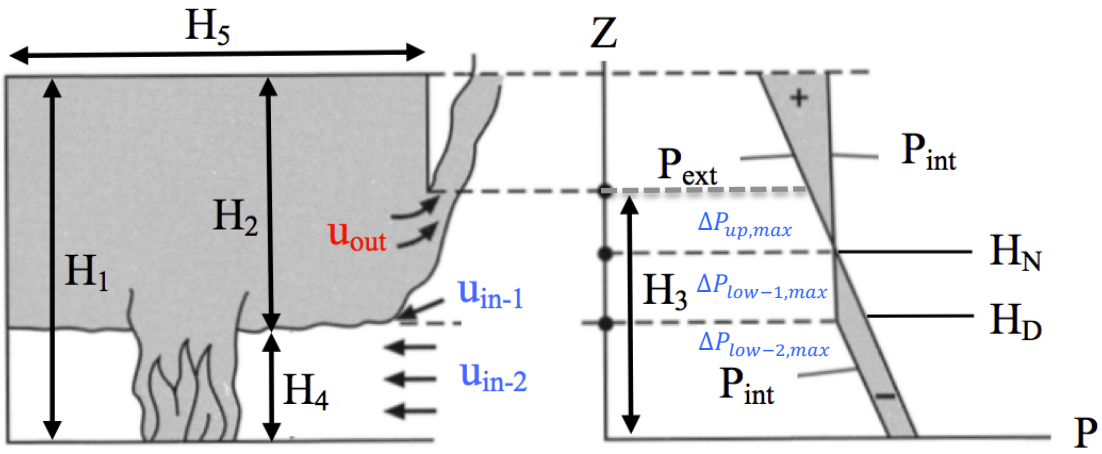

Figure 2-3 Two-layer zone model of internal compartment flows (modified from [25]).

Abbreviations:

H_1 = Compartment Height

H_2 = Smoke Layer Height

H_3 = Ventilation Opening Height

$H_4 = H_D$ = Clean Layer Height

H_5 = Compartment Depth

H_N = Neutral Plane

P_{ext} = Atmospheric Pressure

P_{int} = Internal Compartment Pressure

Above H_N (neutral pressure plane) and along the characteristic length z (along outflow height $0 < z < (H_3 - H_N)$), the maximum pressure difference can be described as [23]:

$$\Delta P_{up,max} = g(\rho_a - \rho_g)(H_3 - H_N)$$ **Equation 2-12**

Below H_N there are two separate characteristic lengths along featuring a linear pressure difference that causes ambient air to entrain [23].

z_1, $(0 < z_1 < (H_N - H_D))$, with a max. pressure difference:

$$\Delta P_{low-1,max} = g(\rho_a - \rho_g)(H_N - H_D)$$ **Equation 2-13**

z_2, $((H_N - H_D) < z < H_N)$, with a max. pressure difference:

$$\Delta P_{low-2,max} = g(\rho_a - \rho_g)H_D$$ **Equation 2-14**

Deduced from the above mentioned pressure differentials, the following equations for the max. characteristic velocities can be inferred [23]:

$$u_{out,max} = \sqrt{2g\left(\frac{\rho_a - \rho_g}{\rho_g}\right)(H_3 - H_N)}$$ **Equation 2-15**

$$u_{in-1,max} = \sqrt{2g\left(\frac{\rho_a - \rho_g}{\rho_a}\right)(H_N - H_D)}$$ **Equation 2-16**

$$u_{in-2,max} = \sqrt{2g\left(\frac{\rho_a - \rho_g}{\rho_a}\right)}H_D$$ **Equation 2-17**

From this two layer-layer zone model, three different max. velocities can be finalised (assuming the internal lower layer is at a different temperature as the ambient temperature): max. exit velocity and max. inflow velocity 1 & 2 [23].

2.2 Regimes of External Fire-Induced Flow

In the previous sections of this chapter internal compartment processes and their interaction with the ambient in terms of temperature, velocity and pressure have been introduced to achieve better understanding of the subsequent external processes of spill plumes exiting compartment openings. In general there are three different plume scenarios that can potentially form upon exiting the fire compartment. These regimes are *attached plume, reattaching plume* and *line plume* and will further be described here. In cases where spill plumes do not exhaust into ambient but enter a cavity space (like in DSF), *fully-developed flow* behaviour can be achieved.

2.2.1 The attached Plume

The scenario of an attaching (also know as adhered plume) plume Figure 2-4 (i) can be considered to be a critical form of window plume in terms of vertical fire spread in buildings due to hot gases and flames directly impinging to the building façade above the opening.

Harrison at al [26] studied a 3-D form experimentally using a $1/10^{th}$ scale model featuring compartment openings of 0.2, 0.4, 0.6, 0.8 and 1.0 m. A variety of total heat output of the fire altered mass flow rate, convective heat flow rate and depth of the hot gas layer below the spill edge. No vertical wall projection (spandrel) along the spill edge has been installed. Instead, the flows generated from the variety of openings were interpreted as a range of possible geometries upstream of the spill edge (e.g. spandrels). Gas flow below the spill edge ranged from relatively cool, shallow and wide to hot, deep and narrow.

It was shown that the 3-D attached plume was highly dependent on the width of the compartment opening. Plumes from wide openings almost immediately attached to the wall Figure 2-4 (i, a) and entrainment of air occurred into the front side and the free ends. Figure 2-4 (i, b) shows that the lateral spread of the plume narrowed before broadening upon end entrainment becoming more significant [26].

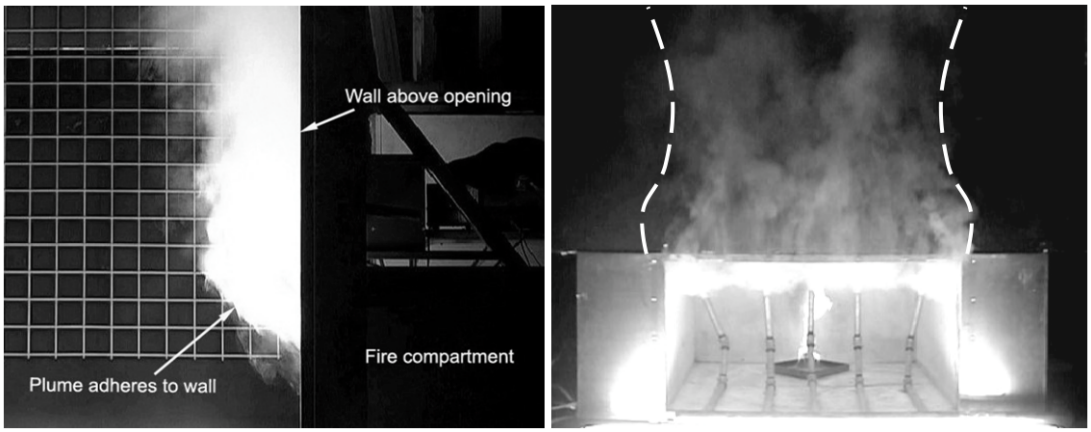

(i)

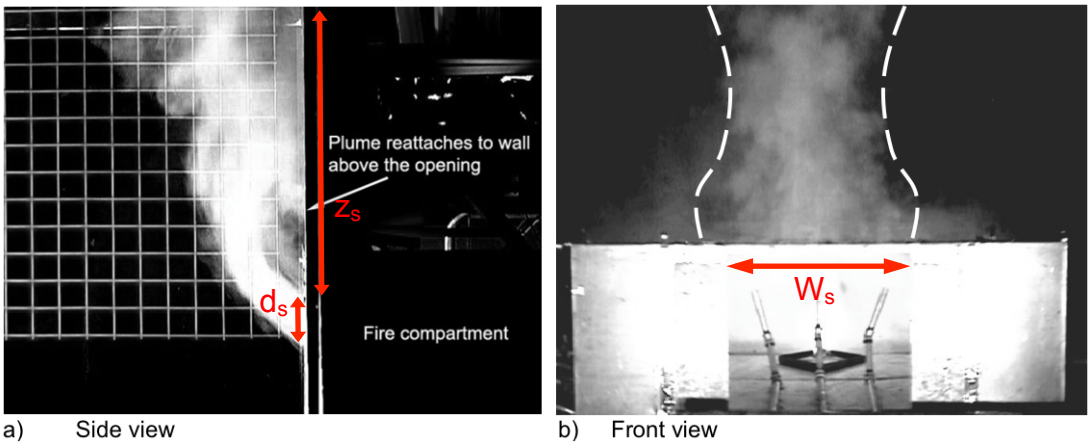

(ii)

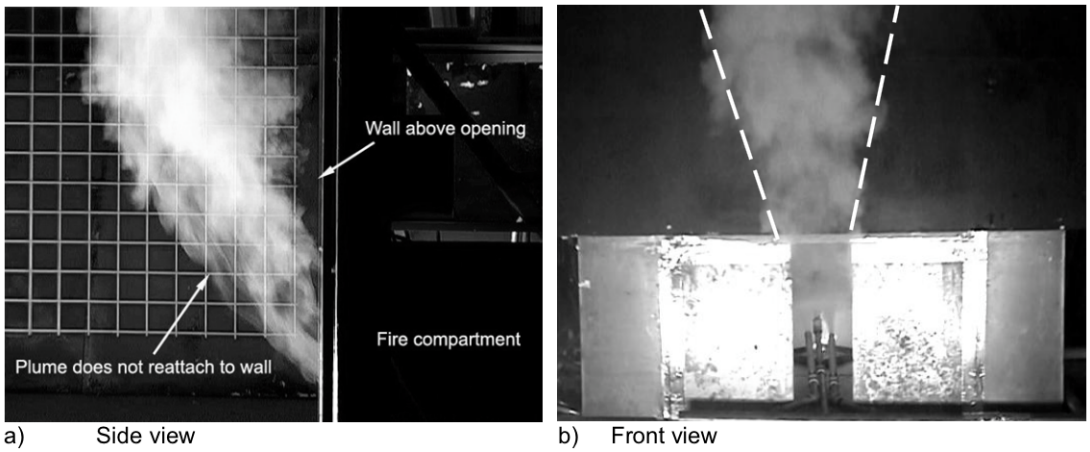

(iii)

Figure 2-4 Characteristic plume scenarios (i) attached, (ii) reattaching, (iii) line plume [26].

2.2.2 The reattaching Plume

This type of plume typically projects horizontally beyond the compartment opening before "curling back" and reattaching to the wall above (Figure 2-4 (ii, a)). Afterwards the plume stays adhered to the façade. In *Harrison's* experiments conditions of intermediate opening width (0.6 to 0.8 m) led to circumstances allowing for a reattaching behaviour. It was observed, that the height of the reattachment above the spill edge increased along with an decreasing compartment opening and when the fire size and depth of the hot gas layer below the spill edge increased. Air entrainment occurred into front and rear of the plume and where it was detached also into the free ends. Upon reattaching, entrainment to the rear stopped [26]. *Zukoski* [14] describes the mechanism of reattachment as being due to the decrease in static pressure between the wall and the plume (in the region of detachment). The pressure drop occurs when the entrainment air supply cannot easily be supplied to the rear of the plume which causes the static pressure to fall close to the wall. The pull back of the plume towards the wall is hence caused by this low pressure region and the effect is known as the *Coanda effect*. As can be seen in Figure 2-4 (ii, b) the lateral extent of the plume narrowed where it detached from the façade due to air entrainment into the rear of the plume (via the ends). Beyond the point of reattachment, the flow broadened again [26].

2.2.3 The Line Plume

When generated from narrow openings, line plumes have been observed to project beyond the opening without reattaching (Figure 2-4 (iii, a)). Air entrainment occurs from both sides and the free ends of the plume (Figure 2-4 (iii, b)). Causes of this projection are increased momentum of the flow from the opening combined with the relative narrow width of the plume not being enough to create a sufficient pressure drop at the rear of the plume. Hence, the *Coanda Effect* does not occur under these circumstances. In contrast to the attached- or reattaching plume, here the lateral extent of the plume broadens above the spill edge [26].

In general, work by *Zukoski* [14] and *Yokoi* [27] considers the outflow layer in terms of the width and depth of the layer flow below the spill edge (W_s and d_s) (see Figure

2-4 (ii, a & b)). The distance above the opening edge where the flow first reattaches to the wall was determined from visual observations (z_{attach}). As Figure 2-5 shows, clear linkage between z_{attach}/W_s and W_s/d_s exists, suggesting that the behaviour of the 3-D plume is dependent on the characteristics of the layer flow below the spill edge (W_s & d_s). No reattaching to the wall above occurred when $W_s/d_s \leq 3$. In cases where $W_s/d_s > 3$, the plume reattached to the façade above and z_{attach} could be determined from data presented in Figure 2-5 by means of the following power law [26].

$$\frac{z_{attach}}{W_s} = 8\left(\frac{W_s}{d_s}\right)^{-2} \rightarrow z_{attach} = \frac{8d_s^2}{W_s} \qquad \textbf{Equation 2-18}$$

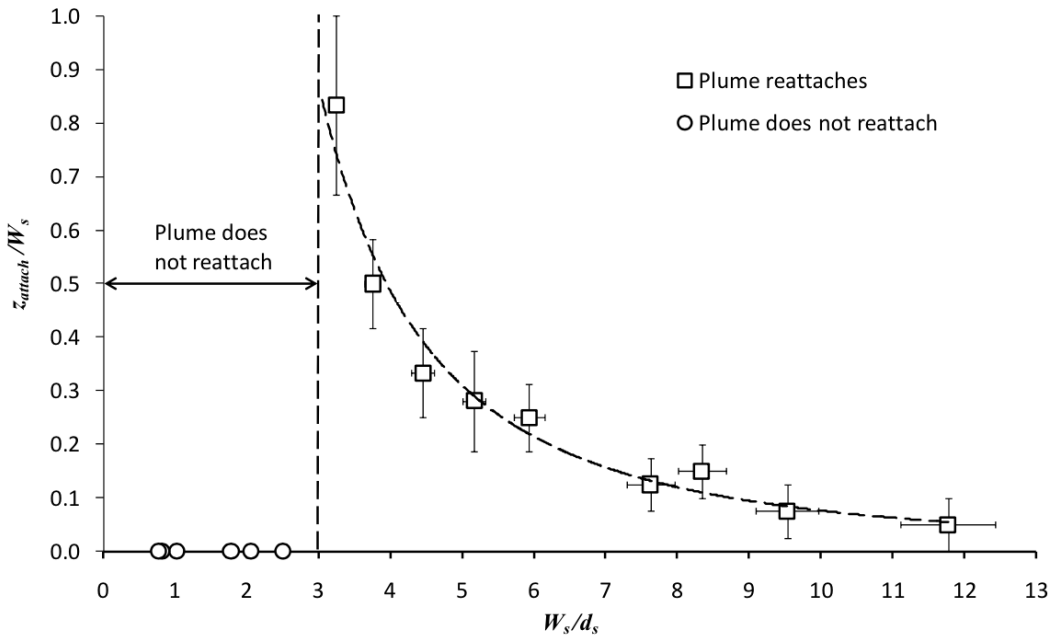

Figure 2-5 z_{attach}/W_s with respect to W_s/d_s [26].

Furthermore, a shape factor *n* of twice the ventilation height divided by the ventilation width is identified to impact the velocity of the spill plume which in return strongly affects its horizontal projection [16].

2.2.4 Fully developed Plume Flow

As is the case when a DSF has been installed, the hot gas spill plume out of the compartment opening cannot immediately exhaust into ambient and dilution processes can not take place in the same manner and magnitude. This section will summarize the conditions needed for the establishing cavity hot gas flow to become fully developed. By its nature, the aspect ratio of DSF structures is large, and in fact, chimney like with usually narrow cavities and tall bounding walls. Hence natural ventilation in theses building features is enforced by the stack effect where the buoyant force allows warm air inside the chimney to rise due to decreased density compared to the ambient air.

2.2.4.1 Stack Effect

In the case of a compartment fire the stack effect amplifies due to the intensely increased temperature difference (i.e. pressure difference) between the hot combustion gases spilling into the cavity space where they rise upwards and eventually get exhausted into ambient and the surrounding ambient air.

Assuming friction losses inside the cavity are negligible is feasible in comparison to the buoyancy-induced pressure differences. Cavity pressure P_{cavity} is due to static forces of the fluid [28]:

$$dP_{cavity} = -\rho_{cavity}\, g\, dz \qquad \textbf{Equation 2-19}$$

where z is the height of the cavity, g the acceleration due to gravity and ρ_{cavity} is the gas density within the cavity (well mixed volume of fire gases and entrainment air). Further assuming constant density and integrating from $z = 0$ to $z = h$ yields:

$$P_{cavity} = P_a - \rho_{cavity}\, g\, h \qquad \textbf{Equation 2-20}$$

where P_a is the pressure at h = 0. Assuming that $P_{cavity} = P_o$ at $h = 0$ and further neglecting wind effects, the pressure outside is P_o:

$$P_o = P_a - \rho_o \, g \, h$$ **Equation 2-21**

where ρ_o is the density outside the cavity. The pressure difference $\Delta P_{cavity/o}$ between inside and outside is expressed as:

$$\Delta P_{cavity/o} = P_{cavity} - P_o = \left(\rho_o - \rho_{cavity}\right) g \, h$$ **Equation 2-22**

Pressure variations inside a building/cavity space being very small in comparison to the atmospheric pressure P_{atm}, the gas density ρ can be calculated from the ideal gas equation:

$$\rho = \frac{P_{atm}}{RT}$$ **Equation 2-23**

where R is the gas constant of air and T the absolute temperature of air. Substituting Equation 2-23 into Equation 2-22 yields:

$$\Delta P_{cavity/o} = \frac{g P_{atm}}{R}\left(\frac{1}{T_o} - \frac{1}{\mathrm{T}_{cavity}}\right)$$ **Equation 2-24**

where T_o is the air temperature outside, and T_{cavity} inside the cavity [28].

2.2.4.2 Fully Developed Flow Characteristics

Fully developed flow regime of an internal flow bounded by walls is discussed here. The boundary can either be in the form of a pipe, or as is the case with DSFs, as a cavity basically consisting of two vertical plates.

As described by [29] in the bounded internal flow viscous effects will grow, meet and permeate the entire flow. In the entrance region, L_e, the almost inviscid upstream

flow converges and enters the duct. From the point of entry viscous boundary layers grow downstream, hindering axial flow *u(r, x)* at the wall whilst accelerating the centre flow in order to maintain the incompressible continuity requirement.

$$Q = \int u \, dA = const \qquad \textbf{Equation 2-25}$$

A certain distance downstream from the entrance, the boundary layers merge and the inviscid centre vanishes. Then the tube flow is completely viscous and the axial velocity changes slightly further until $x = L_e$ from where on the it no longer changes with x and is said to be fully developed. Hence, velocity only changes with respect to r. Further downstream the velocity profile is constant, the wall shear is constant, pressure drops linearly with respect to x for laminar and turbulent flow [29].

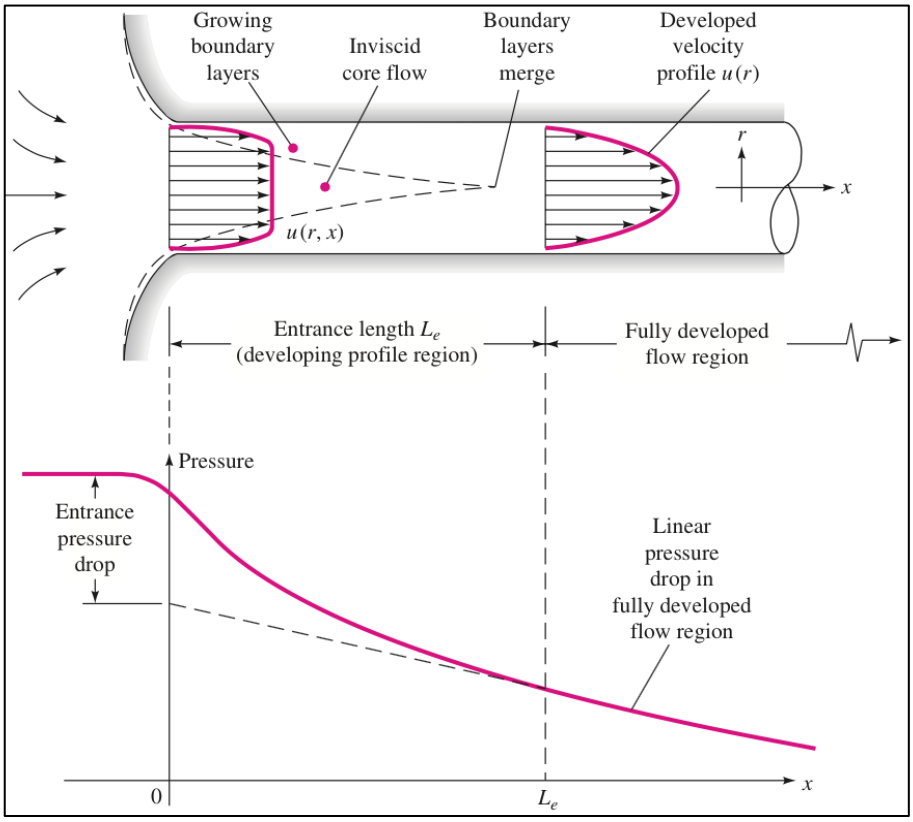

Figure 2-6 Velocity profiles and pressure distribution at the entrance of a pipe flow [29].

The only parameter affecting the entrance length is the *Reynolds* number, *Re,* which forces L_e to be shorter due to faster growing (expanding) boundary layers. Accepted correlations for laminar and turbulent flow are [29]:

$$\frac{L_e}{d} \approx 0.06\, Re_d \; (laminar) \qquad \textbf{Equation 2-26}$$

$$\frac{L_e}{d} \approx 1.6\, Re_d^{1/4} \quad for \quad Re_d \leq 10^7 \; (turbulent) \qquad \textbf{Equation 2-27}$$

2.2.4.3 Thermal Plume Development in Cavities

Only very limited information on plume development between vertical plates (i.e. cavities) is available. The lack of information motivated work by *Zinoubi* [30] studying the development of an axisymmetric plume (symmetry along the vertical centreline of the plume, air entrainment from all directions) between vertical plates. The flow within the 0.15 m gap (square plates 0.4 x 0.4 m, heated by carbon paper resistance to 323 K) was generated by a hot plate (flat disc) at 573 K and three different flow zones have been identified. Close to the source the zone is described as unstable and eddy formation has been observed. This is followed by a intermediate zone of flow development and a last zone at the cavity outlet described to feature fully developed turbulent flow.

Based on the same methodology, *Naffouti et al* [31] investigated the effect of spacing between vertical plates of a parallelepipedic channel on average thermal and dynamic fields of a thermal plume. The experimental setup is analogous to the studies by [30] but with the heat source this time being a rectangular block spanning over the entire channel depth of 0.4 m. Cavity widths ranged from 0.075 m (e_1), 0.11 m (e_2), 0.15 m (e_3) to 1.8 m (e_4) (Figure 2-7). Here, spacing e_4 can be interpreted as a free, unbounded thermal plume in a large ambient medium where thermosiphon flow (natural convection heat exchange) is not present and interactions between plates and plume can be neglected. The developing flows between the plates have been studied in three locations downstream of the source ($Z^* = 0.10$, $Z^* = 0.37$ and $Z^* = 0.92$).

Figure 2-8 (a - c) shows the transverse average dimensionless temperature of the flow three sections (Z^*) plotted against the spacing. Close to the heat source (Figure 2-8 (c)) the narrowest cavity (e_1) shows a practically uniform temperature profile

with only very light variations of the thermal gradient. Upon increase of the spacing, profiles narrow and temperature peaks locate on the plume axis. Generally high horizontal thermal gradients on this level suggest the dominance of the thermal plume.

Figure 2-8 (b) depicts the intermediate level of the cavity flow and a general decrease of the temperatures. Due to the reduction of spacing profiles flatten. Towards the cavity walls, temperature increases from the Joule effect (heat from electric current through conductor) and radiation emitted by the heat source.

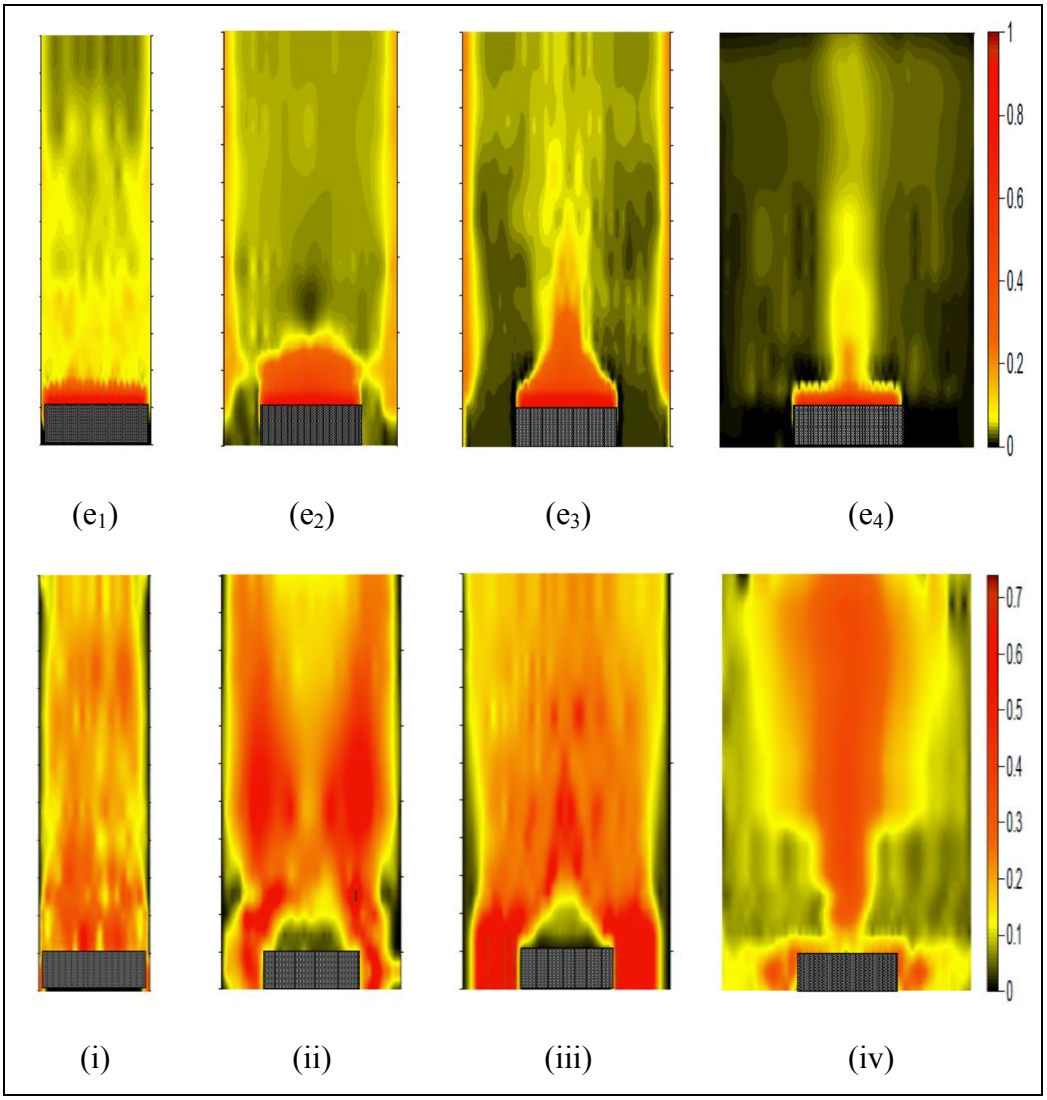

Figure 2-7 Dimensionless average temperature of the cavity flow in configurations e_1 - e_4 and the dimensionless average vertical component velocity of the flow for configurations e_1 - e_4 (i - iv) [31].

At the channel top (Figure 2-8 (a)) thermal profiles flatten except for the largest spacing which can be seen as a free plume. This can also be observed from the dimensionless average temperature plot (e_4) in Figure 2-7. For all other cases this indicates temperature uniformity in the channel centre at the exit.

Analogue to the temperature profiles, Figure 2-8 (i - iii) illustrates the average vertical velocity component of the flow for the variety of spacing. Near the source (Figure 2-8 (iii)), especially spacing e_2 and e_3 show an intensification of the dynamic gradients on both sides of the source due to the thermosiphon effect accelerating the ascending flow (see also Figure 2-7 (ii) & (iii). The drastically decreased velocities in the vicinity of the median plane proves existence of a weak circulation region. This effect cannot be seen in the widest spacing of e_4, where velocities increase in the channel centre.

At the channel top a homogenisation of the flow can be seen in e_1 and e_3 by relatively uniform velocity profiles.

It has been concluded that the inter-plate spacing is the most important parameter affecting thermal and dynamic behaviour of the plume within the channel [31].

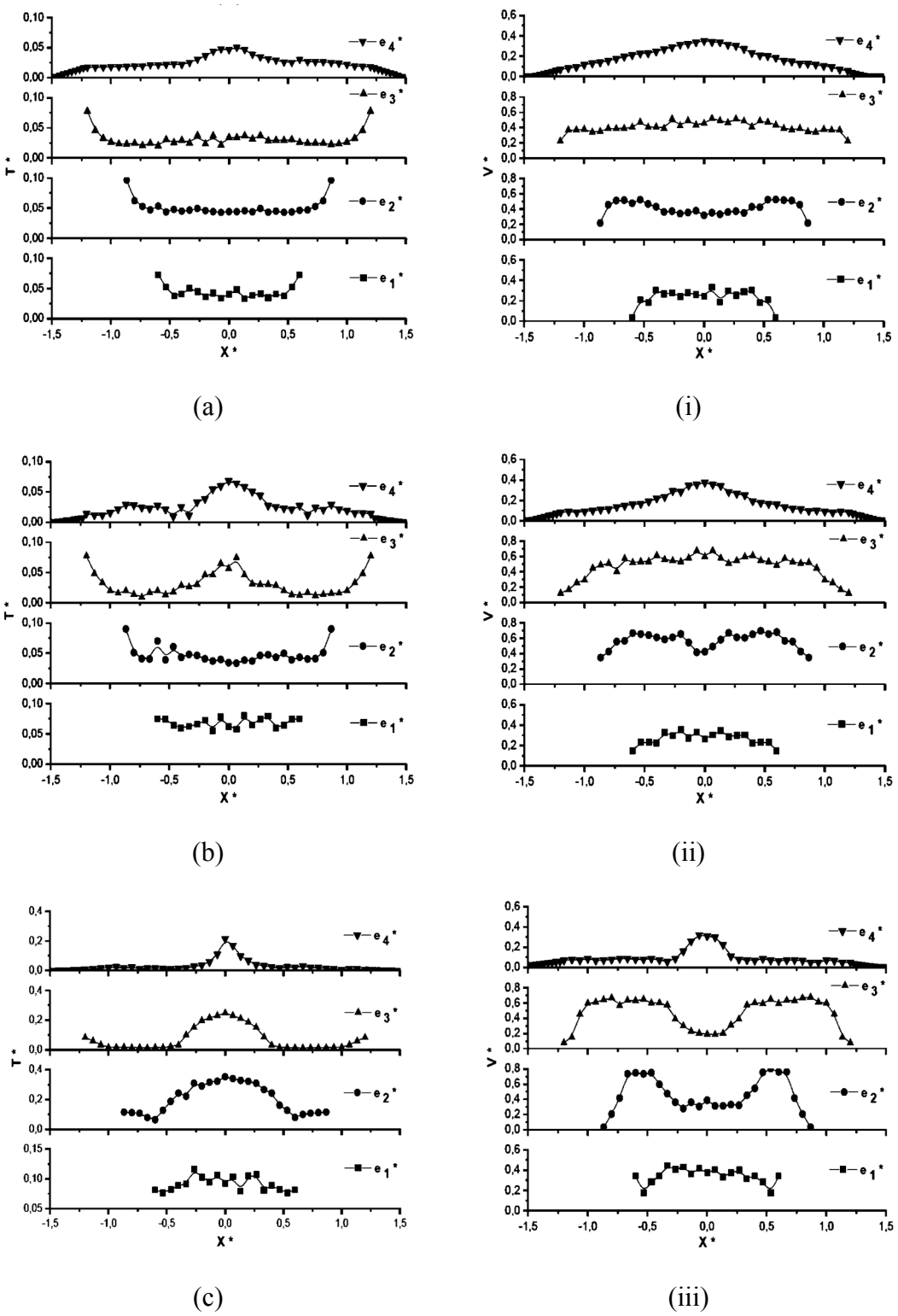

Figure 2-8 Transversal distribution of the dimensionless average temperature of the flow *vs* spacing for Z* = 0.10 (c), Z* = 0.37 (b) and Z* = 0.92 (a). Transversal distribution of the dimensionless average vertical component velocity of the flow *vs* spacing for Z* = 0.10 (iii), Z* = 0.37 (ii) and Z* = 0.92 (i) [31].

2.3 Preliminary Observations and Summary

Chapter 2 has outlined the physical processes involved in post-flashover compartment fires and the interactions with the ambient atmosphere. The criteria of the spill plume regimes *attached*-, *reattaching*- and *line plume* are given and *fully developed* characteristics in terms of a DSF flow are presented. Finally, thermal plume development between vertical parallel plates is described by means of an experimental study which suggests that inter-plate spacing is the single most important factor in the development of a cavity flow.

3 Salt-Water Modelling Experiments

3.1 Literature Review

Physical scale modelling such as salt-water modelling (SWM) has in the past been used to mimic large-scale experiments too complex to study economically by other means. *Sangras & Faeth* [32] utilized SWM to study the temporal development of round turbulent non-buoyant starting jets and puffs and buoyant starting plumes injected vertically downward into still and unstratified fresh water. The measurements were obtained as a function of time from colour video records. This early technique does not allow for a quantitative analysis of concentrations within the flow field but is sufficient in estimating front arrival times.

Steckler et al [33] used the technique to demonstrate the feasibility of analysing hot gas flows inside a $1/20^{th}$ scale model war vessel. Scaling relations connecting reduced-scale salt-water flows to full-scale hot gas flows have partially been validated for specific geometrical arrangements by comparing the layer interface heights. It was shown that scaling of the governing equations for dimensionless temperature and salt-water concentration have essentially identical form except for *Re, Sc* and *Pr* discrepancies encountered in the diffusive term coefficients. However, salt-water experiments cannot simulate heat transfer near the enclosure boundaries by means of salt transfer. Buoyancy is maintained for a longer period compared to real fire experiments and therefore the technique can be considered to be a more conservative approach in multi-compartment structures where speed and spatial extend of the flow are likely to be greater than in real fire experiments.

Clement & Fleischmann [34] conducted a series of salt-water experiments trying to imitate early stage smoke flow in a residential building fire. Laser Induced Fluorescence LIF was used to measure the fluid density of the salt-water flow field. These experiments where then modelled using the Large Eddy Simulation (LES) and Direct Numerical Simulation (DNS) techniques of the Fire Dynamics Simulator (FDS). The study showed at high grid resolutions satisfactory agreement between experimental work and LES computational results.

Jankiewicz [35] studied the prediction of smoke detector response times using SWM and Planar Laser Induced Fluorescence (PLIF). Comparing these results to the actual response times from a full-scale experiment, agreement of the models prediction has been found.

Yao [36] found successful agreement between PLIF experiments, real fire plume measurements and McCaffrey's plume theory, further establishing the applicability of the PLIF salt-water measurements and scaling techniques for unconfined fire plumes. Additionally measurements for a CFD model validation have been obtained within this study and salt-water measurements were compared with real fire measurements and ceiling jet theory.

Siang [37] validated the use of SWM as a diagnostic, predictive and scaling tool to study smoke spread in a compartment featuring a beamed ceiling. Here PLIF has been combined with Particle Image Velocimetry (PIV) and dimensionless dispersion signatures and front arrival times were compared to real fire and salt-water experiments showing agreement.

3.1.1 Summary

Literature suggests SWM has initially been applied as a more economic method to imitate complex large-scale experiments despite its limitation to simulate heat transfer close to enclosure boundaries. With advances in scaling techniques and measurement resolution and precision it can nowadays be used to validate CFD models and real fire experiments.

3.2 Research Objectives

The herein proposed experimental framework aims to establish an experimental strategy analysing fire-induced flows in double-skin facades by the use of small scale SWM and large scale fire experiments. The application of PIV on a small scale allows for highly detailed flow characterisation which, under real fire conditions, would only be achievable with considerably increased effort and expense. Here, as in many other instances, laser-assisted diagnostics are the only unobtrusive method to investigate fluid flow. Within the experimental framework, salt-water flows between two vertical plates mimicking a DSF, are being studied in terms of velocity whilst

changing parameters like cavity width and spandrel height. As mentioned before, one limitation to this technique is the inability to simulate heat transfer to boundary walls. This differs from real fire circumstances where heat transfer occurs to the cavity glazing but can be neglected as the HRR is much larger than the heat losses through the glass.

Results are compared to real fire experiments in a qualitative manner. These large-scale tests have been set to measure incident heat flux to either face of a DSF setup. Finally, small- and large-scale experiments will be compared by the use of dimensionless analysis.

Specific Objectives:

- Characterize quantitatively the influence of cavity width and spandrel height on the velocity distribution in DSFs using small-scale SWM.
- Investigate quantitatively the influence of cavity width on the heat flux distribution within a DSF by the use of large-scale fire experiments.
- Develop a methodology to qualitatively link results of the above mentioned experimental work using dimensionless analysis.

3.3 Principles of Salt-Water Modelling

As *Yao* [36] summarizes, SWM is based upon fundamental similarities between fire-induced flows and salt-water flows and can be used as a tool to characterise different aspects of fire-induced flow like heat transfer, dispersion and turbulent mixing. SWM applies buoyant scale analysis and flow experiments combined with laser diagnostics.

The modelling analogy between fire-induced and salt-water flows has been established based on the similarity of dimensionless groups (DG) governing the linking equations. *Quintiere* [38] developed the basic scaling theory for fires using DGs derived from the governing differential equations. The proposed scaling method also finds application in the study at hand where salt-water flow is injected into a fresh-water environment. This allows the injection source to act as buoyant heat

source similar to a fire source. Here, the salt-water mass species and momentum equations correspond to the momentum and energy equations in the fire system.

3.3.1 Dimensionless Analysis

Yao [36] further recapitulates the dimensionless governing equations of fire-induced flow and salt-water flow with the corresponding dimensionless (dl) parameters.

3.3.1.1 Fire-Induced Conservation Equations

Momentum:

$$\frac{\partial u_j^*}{\partial t^*} + u_i^* \frac{\partial u_j^*}{\partial x_i^*} = -\frac{\partial \mathrm{p}^*}{\partial x_i^*} + \frac{1}{(Gr_{source}^{fire})^{1/3}} \frac{\partial^2 u_j^*}{\partial x_i^* \partial x_i^*} + \theta_T^* \cdot f_j^* \qquad \textbf{Equation 3-1}$$

Energy:

$$\frac{\partial \theta_T^*}{\partial t^*} + u_i^* \frac{\partial \theta_T^*}{\partial x_i^*} = \frac{1}{(Gr_{source}^{fire})^{1/3} Pr} \frac{\partial^2 \theta_T^*}{\partial x_i^* \partial x_i^*} + \dot{q}^* \qquad \textbf{Equation 3-2}$$

where,

- dl. time $t^* = t_{fire}(g/L_f)^{1/2}(Q^*)^{1/3}$
- dl. position $x_i^* = x_i/L_f$
- dl. source strength parameter $Q^* = \beta_T Q\left(\rho_0 c_p g^{1/2} {L_f}^{5/2}\right)^{-1}$

where, $\beta_T = {}^{1}/_{T_0}$

- dl. velocity $u_j^* = u_j\left(gL_f\right)^{-1/2}(Q^*)^{-1/3}$
- dl. density difference $\theta_T^* = \beta_T(T - T_0)(Q^*)^{-2/3}$
- dl. pressure $p^* = p(Q^*)^{-2/3}(\rho_0 g L_f)^{-1}$

- body force $f_j^* = (0, 0, -1)$
- volumetric energy release rate $\dot{q}^* = \dot{q}''' L_f^3 \dot{Q}^{-1}$
- dl. Grashof no. (source based) $Gr_{source}^{fire} = g\beta_T \dot{Q} L_f^2 / \rho_0 c_p \upsilon^3$
- Prandtl number $Pr = \upsilon / \alpha$

3.3.1.2 Salt-Water Conservation Equations

Momentum:

$$\frac{\partial u_j^*}{\partial t^*} + u_i^* \frac{\partial u_j^*}{\partial x_i^*} = -\frac{\partial p^*}{\partial x_i^*} + \frac{1}{(Gr_{source}^{sw})^{1/3}} \frac{\partial^2 u_j^*}{\partial x_i^* \partial x_i^*} + \theta_{sw}^* \cdot f_j^* \qquad \textbf{Equation 3-3}$$

Salt Mass Species:

$$\frac{\partial \theta_{sw}^*}{\partial t^*} + u_i^* \frac{\partial \theta_{sw}^*}{\partial x_i^*} = \frac{1}{(Gr_{source}^{sw})^{1/3} Sc} \frac{\partial^2 \theta_{sw}^*}{\partial x_i^* \partial x_i^*} + \dot{w}_{sw}^* \qquad \textbf{Equation 3-4}$$

where,

- dl. time $t^* = t_{sw} (g / L_{sw})^{1/2} (m_{sw}^*)^{1/3}$
- dl. position $x_i^* = x_i / L_{sw}$
- dl. source strength param. $m_{sw}^* = \beta_{sw} \dot{m}_{salt} \left(\rho_0 g^{1/2} L_{sw}^{5/2} \right)^{-1}$

  where, $\beta_{sw} = 0.76$

- dl. velocity $u_j^* = u_j (g L_{sw})^{-1/2} (m_{sw}^*)^{-1/3}$
- dl. density difference $\theta_{sw}^* = \beta_{sw} Y_{salt} (m_{sw}^*)^{-2/3}$
- dl. pressure $p^* = p (m_{sw}^*)^{-2/3} (\rho_0 g L_{sw})^{-1}$
- body force $f_j^* = (0, 0, -1)$

- vol. energy release rate $\dot{w}^*_{sw} = \dot{w}'''L^3_{sw}\dot{m}^{-1}_{salt}$
- dl. *Grashof* no. $Gr^{sw}_{source} = g\beta_{sw}\dot{m}_{salt}L^2_{sw}/\rho_0\upsilon^3$
- Schmidt number $Sc = \upsilon/D$

The dimensionless source strength Q^*, which has first been introduced in the fire-induced flow, is the analogue of the dimensionless source strength in the salt-water flow m^*_{sw}. The salt mass flux being introduced into the flow governs its source strength. Here, β_{sw} (= 0.76) is a constant describing the relationship between salt mass fraction and salt-water density. In fire-induced flows, β_T is the thermal volumetric expansion coefficient equal to $1/T_0$ which originates from the ideal gas state equation for flows with small density changes. For the non-dimensionalisation, not the Reynolds number, but the *Grashof* number is used since it can be expressed in terms of the driving flow heat or mass source. The relationship between the *Re* and the source based *Gr* can be established if the velocity scale is given by the characteristic velocity of the plume $U = (Q^*)^{1/3}(gL)^{1/2}$ which shows that $Re = Gr^{1/3}$.

The dimensionless forms of the momentum equations for fire-induced and salt-water flow are identical as can be seen in

$$\frac{\partial u^*_j}{\partial t^*} + u^*_i\frac{\partial u^*_j}{\partial x^*_i} = -\frac{\partial \mathrm{p}^*}{\partial x^*_i} + \frac{1}{(Gr^{fire}_{source})^{1/3}}\frac{\partial^2 u^*_j}{\partial x^*_i \partial x^*_i} + \theta^*_T \cdot f^*_j \qquad \textbf{Equation 3-1}$$

and

$$\frac{\partial u^*_j}{\partial t^*} + u^*_i\frac{\partial u^*_j}{\partial x^*_i} = -\frac{\partial p^*}{\partial x^*_i} + \frac{1}{(Gr^{sw}_{source})^{1/3}}\frac{\partial^2 u^*_j}{\partial x^*_i \partial x^*_i} + \theta^*_{sw} \cdot f^*_j \qquad \textbf{Equation 3-3}$$

Similar form of the dimensionless transport equations of energy and salt mass species (in fire and salt-water) is shown in

$$\frac{\partial \theta_T^*}{\partial t^*} + u_i^* \frac{\partial \theta_T^*}{\partial x_i^*} = \frac{1}{(Gr_{source}^{fire})^{1/3} Pr} \frac{\partial^2 \theta_T^*}{\partial x_i^* \partial x_i^*} + \dot{q}^* \qquad \textbf{Equation 3-2}$$

and

$$\frac{\partial \theta_{sw}^*}{\partial t^*} + u_i^* \frac{\partial \theta_{sw}^*}{\partial x_i^*} = \frac{1}{(Gr_{source}^{sw})^{1/3} Sc} \frac{\partial^2 \theta_{sw}^*}{\partial x_i^* \partial x_i^*} + \dot{w}_{sw}^* \qquad \textbf{Equation 3-4}$$

Using a source based non-dimensionalisation approach allows the definition of the dimensionless density difference θ_T^* and θ_{sw}^* to be analogous. This can also be expected once the boundary conditions of fire induced and salt-water flow are matched. Unconfined flows (e.g. upper sections of the injected salt-water plume in the here presented experiments) do not require boundary conditions to be taken into account. However, interpretation is needed if obstructions of any kind lie in the flow path. Since the boundary condition in the experiments at hand does not allow for mass fraction gradients to establish, the similarity to adiabatic boundary conditions in fire conditions is given.

Work conducted by [38] [39] [40] shows that scaling methods are not able to match all of the key dimensionless groups under all circumstances which can cause discrepancies between flow in scaled models and real flow. Differences in the *Gr, Pr* and *Sc* numbers between fire and salt-water conditions are able to cause the flow to behave differently. By assuring that the *Gr* is sufficiently large (turbulent flow character in fire and salt-water), diffusion on a molecular scale will be negligible compared to the turbulent mixing. This does not keep true for conditions close to boundary walls where velocity and energy gradients are steep and the diffusive terms might not be negligible. For fully turbulent flow, *Yao* [36] finds good agreement between fire and salt-water results and suggests the effects caused by differences between theses parameters are negligible.

Layton [41] mentions a $Gr > 10^9$ to be sufficient so that flow in confined and unconfined configurations is turbulent with good agreement between fire and salt-water tests.

3.4 Description of the Experiments

The SWM experiments have been conducted in the laboratories of the *Department for Fire Protection Engineering at the University of Maryland* where earlier work by [42] [41] [35] [36] [43] already applied similar methodologies to study salt-water flows. Apart from the originally intended work, the project at hand also aimed to improve precision of the current test setup.

3.4.1 Experimental Setup

The experiment consists of six main parts which are shown in Figure 3-1. The initial salt-water flow is delivered by a gravity-fed salt-water supply system (Figure 3-2) which is designed to hold a constant gravity head. The system consists of an upper and lower 10 gallon (37.85 L) storage container in which the salt-water solution is mixed and particles and water conditioning substances are added to the volume. A custom built mixing device and the constant flow through the pipe system assists the mixing process and ensures the added nanoparticles do not settle. Additives like Rhodamine 6G break down when exposed to UV light, hence the supply system has been encased in black plastic sheets to block the surrounding light. Additionally, dechlorination agent was added to stop chlorine in the tab water breaking down the Rhodamine 6G.

The salt-water mixture is then injected into the fresh-water tank via a 5.6 mm diameter stainless steel tube which was fed by a 1000 ml/min flow meter, set to 180 ml/min in the experiments presented within this project. Identical injection source conditions have in-depth been analysed and described by *Layton* [41] using a correlation of valid enclosure height as a function of salt-water mass flow rate based on McCaffrey's plume. The presented selection of height vs source strength has been calculated to follow the appropriate power laws for centreline density difference and velocity.

The unconfined plume source and settings of the diagnostics are described in Table 3-1 since the source itself was placed outside the field of view (FOV) in the authors experiments and could not be recorded nor described. This is due to the focus of the

experiments not being on the injection source description but the cavity flow away from the point source. The sharpness fall off towards the edges of the lenses set at extremely wide f-stops would additionally have hindered clean measurements.

here, Figure 3-3 describes a schematic of the 800 x 700 x 300 mm sized acrylic model that has been built out of clear acrylic sheets to serve as an imitation of a real fire compartment attached to a DSF. Hot combustion gases (i.e. the turbulent salt water plume) gets injected via the compartment top (i.e. bottom) and spills over a spandrel and out of the non-existent interior glass (i.e. acrylic) pane into the cavity space where the salt/fresh-water mixture sinks to the bottom of the large experimental tank.

Figure 3-4 (a) shows the actual test rig with supporting aluminium frame structure and Figure 3-4 (b) a close-up of the compartment during testing. The firing laser sheet excites the particle-laden salt-water flow and the acrylic sheet. Sheet and surrounding substructure are subtracted from the post-processing analysis later on and have no influence on the overall results.

Diagnostics	PIV + PLIF
Number of Frames	300
Injector	5.6 Tubular
FOV [mm]	350
Camera	- Imager ProX 4M / ImagerIntense
Lens	- 60 mm f2.8 / 35 mm f2.0
Exposure [s]	0.008
Laser Interval *dt* [ms]	5500
Volumetric Flow Rate [L/m]	0.18
Injection Velocity [mm/s]	122
Salt Mass Fraction	0.07
Char. Length Scale D^* [mm]	1.2
Virtual Origin (theta) [mm]	- 0.008
Virtual Origin (u_3) [mm]	0.018
$\dot{m}_{salt}$ **[g/s]**	0.22
Re_D	679

Table 3-1 Injection source characteristics and diagnostics settings [41].

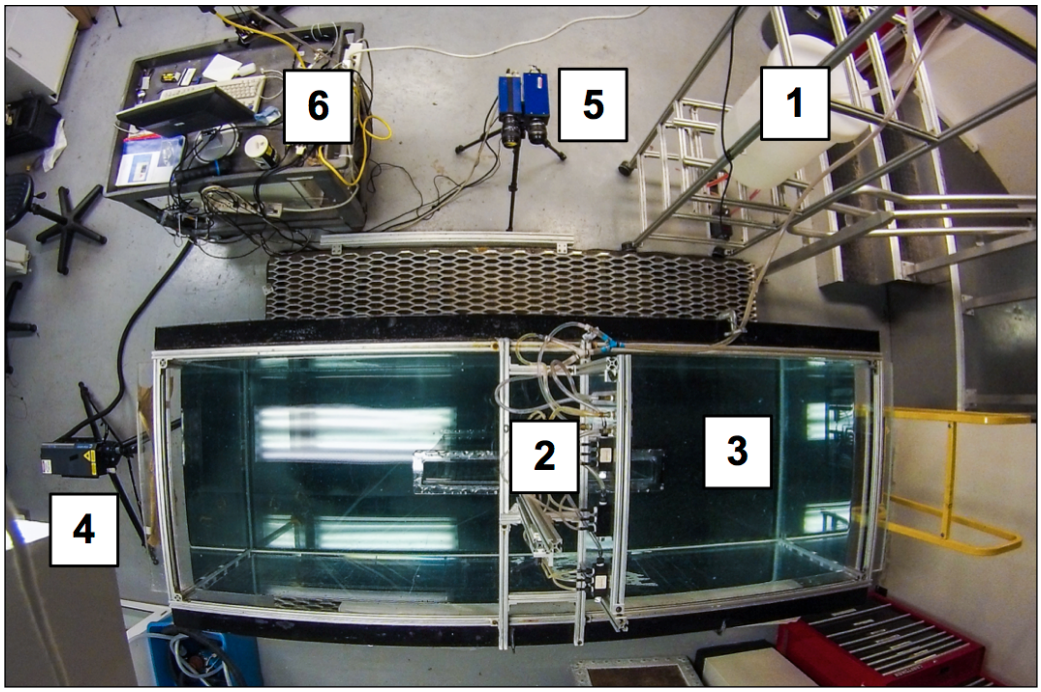

Figure 3-1. SWM experimental setup and environment: (1) salt-water storage & preparation, (2) salt-water injection & model, (3) fresh-water tank, (4) Nd/YAG laser, (5) camera setup, (6) data processing.

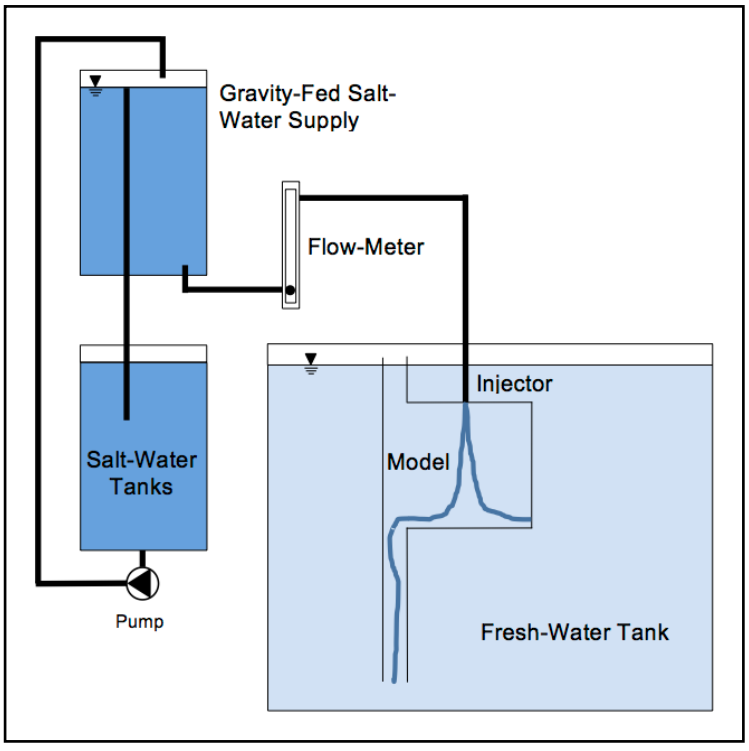

Figure 3-2. Experimental setup (fluids & model).

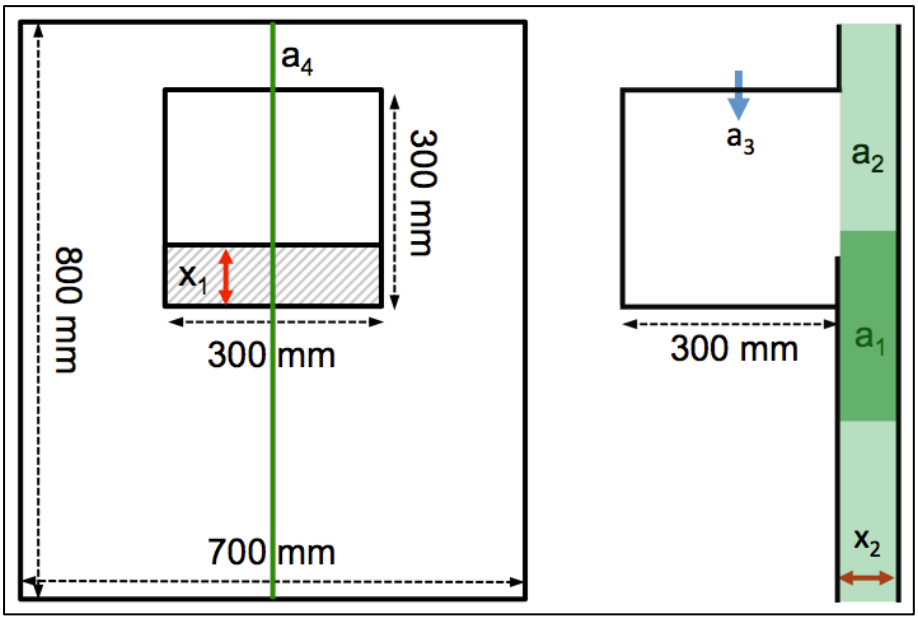

here, Figure 3-3. Acrylic scale-model of a DSF. Front- (left) and side view (right): (x_1) variable spandrel height, (x_2) variable cavity width, (a_1) spill zone measurements, (a_2) entire cavity measurements, (a_3) injector position, (a_4) laser sheet location.

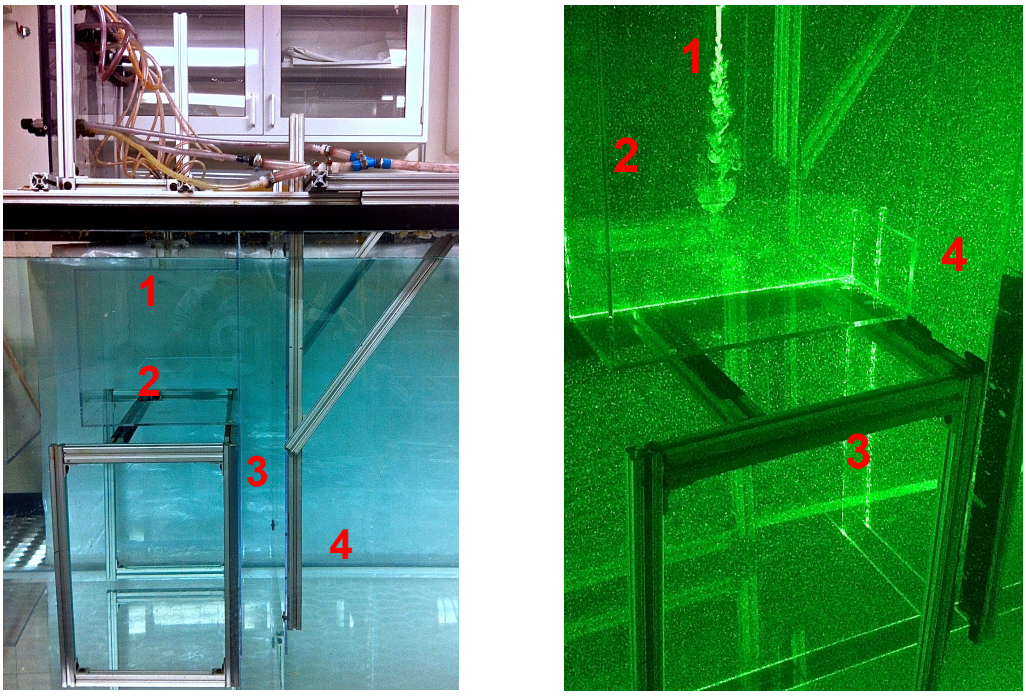

(a) (b)

Figure 3-4 Acrylic DSF test rig and injection system (a). Close-up on Nd/YAG laser sheet during testing (b). (1) injection point, (2) compartment interior, (3) cavity space, (4) ambient fresh-water

3.4.2 Imaging and Laser Diagnostics

The SWM experiments have been documented by a twin-camera setup consisting of dedicated cameras for PIV and PLIF. However, only the PIV data will be presented within this project since the additional information of the PLIF system was deemed not valuable.

In order to be able to track nanoparticles in PIV, a LaVision ProX 4M camera has been chosen which features a resolution of 2048 x 2048 pixels. The sensor size was 15.6 mm x 15.3 mm with single pixels at 7.4 x 7.4 μm^2. The imaging frequency for double-frame PIV was set to 5 Hz. A 60 mm, f1:2.8 lens was used in combination with the CCD camera and set to a FOV of 350 mm.

To excite and visualise the particle laden salt-water flow, a 30 mJ double-pulse 532 nm Nd/YAG laser has been used. The time between the two pulses *dt* (resp. PIV images) determines the extent to which a particle moves between two images. As will be explained at a later stage, tracking of this movement allows establishing of flow vectors and velocities.

3.4.3 Particle Image Velocimetry (PIV)

In the following section, the fundamental features of this widely used methodology will be described as performed, amongst others, by *Raffel* [44]. The PIV setup consists of a number of sub-systems and to most, as well as the SWM experiments, tracer particles have to be added. Here, these are neutrally buoyant, silver coated hollow microspheres which get excited by the Nd/YAG laser pulses. The reflecting light from the particles gets recorded by a single or multiple frames using imaging diagnostics. Particle displacement between images/laser pulses can be tracked and evaluated using sophisticated post-processing.

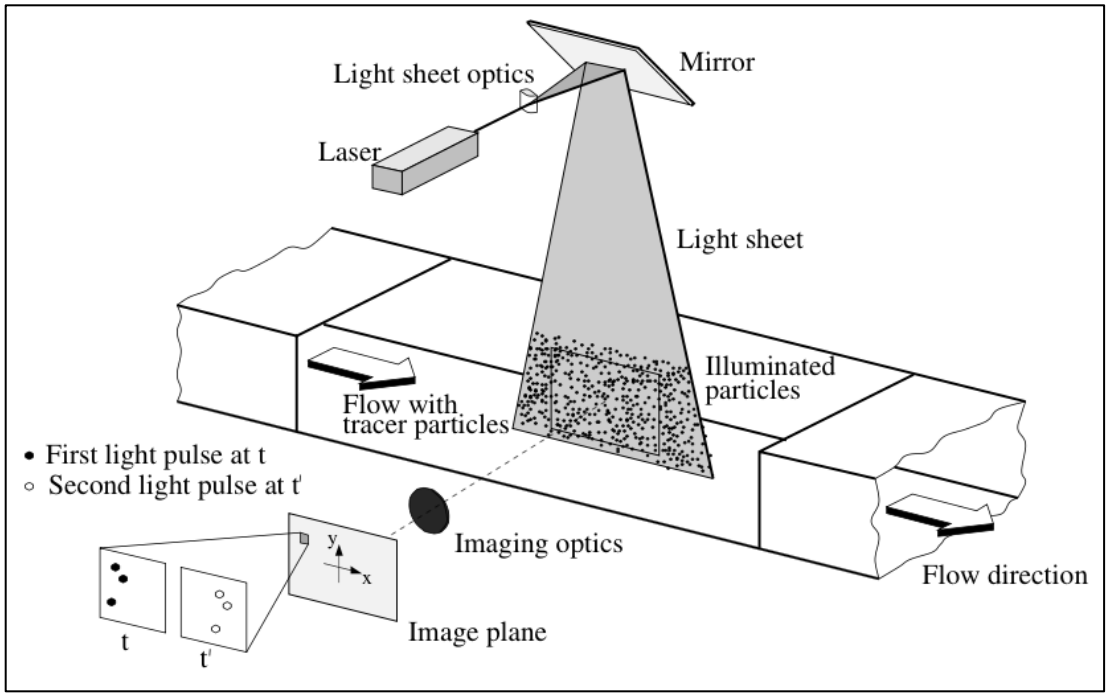

Figure 3-5 Simplified PIV arrangement [44].

Figure 3-5 illustrates the fundamental principle of PIV regardless of the type of fluid flow (gaseous/liquid). Tracer particles in the flow are illuminated twice by a light sheet (laser/LED) as seen in Figure 3-4 (b) . This time delay between images depends on the mean flow velocity and the chosen imaging magnification. This is one reason why the presented experiments were not able to record plume flow at the source and cavity flow simultaneously since the discrepancy between both velocity profiles was too large. The scattered light from the tracer particles is recorded by a cross-correlation digital camera with a 532 nm band pass filter to block light of other, unrelated, wavelengths.

During pre- and post-processing the following routine has been applied :

1. normalise seeding particle intensity
2. subtract image background
3. cross-correlation particle tracking (set interrogation region (here, here, Figure 3-3 (a_2)), track across *dt*)
4. establish initial vector for guidance
5. decrease size of interrogation region, increase resolution and accuracy

As summarized by *Layton* [41], *Keane and Adrian* [45] developed a Monte Carlo simulation and identified a set of non-dimensional parameters that are significant in optimizing PIV performance. First of all, the particle image density shall be larger than 10.

$$N_I > 10 \qquad \textbf{Equation 3-5}$$

This assures that there are sufficient particles per image to acquire meaningful data. The relative in-plane image displacement per particle should be less than ¼ of the width of the total interrogation region to minimize errors due to long-distance mismatching.

$$|\Delta X| < \frac{1}{4} d_I \qquad \textbf{Equation 3-6}$$

Relative out-of-plane displacement shall be less than ¼ the thickness of the laser (or LED) light sheet, again to reduce errors and increase accuracy.

$$|\Delta z| < \frac{1}{4} \Delta z_0 \qquad \textbf{Equation 3-7}$$

Finally, the local variation of displacements shall be less than $1/20^{th}$ the size of the interrogation region.

$$M|\Delta u|\,\Delta t/d_I < 0.05 \qquad \textbf{Equation 3-8}$$

where,
M = chip size / field of view

The already mentioned tracer particles (d = 50 μm) and their density was chosen such that there was a sufficient number of particles left at the downstream locations

of interest (e.g. DSF model cavity) without reaching the speckle regime. Beyond this point, a too high particle density reflects too much light off the seeding and causes scatter light to appear as real particles which then produce errors in post-processing. Speckle regime has been reached within the direct vicinity of the injection source (60 mg/L) to ensure sufficient particle density downstream and inside the cavity after mixing processes caused dilution of the initial salt-water flow. The ambient fresh-water volume has been seeded with 20 mg/L.

Similar to the experiments of [41], camera properties and tracer particles need to be matched in a way that the approximate size of one particle corresponds to 2 pixels on the camera sensor to avoid "peak locking", which prohibits correct interpolation of peak intensities between pixels and displacement calculations.

Pixel size estimate:

$$d_i = \sqrt{(Md_p)^2(d_{diff})^2} \qquad \textbf{Equation 3-9}$$

where,

d_p = seeding particle mean diameter, = 50 μm

$d_{diff} = 2.44 \cdot f(M+1)\lambda$

where,

f = F-Stop on the camera lens

λ = is the wavelength of incident light [m]

In actuality, the pixel size was slightly above the calculated 2-pixel threshold.

3.5 Overview of Experiments

As shown in Table 3-2, a total of 12 experiments have been designed to cover a sufficient range of potential flow scenarios. The dependence of a secondary parallel vertical plate on the flow pattern was realised in *tests 1 to 9*.

Test	Cavity Width [mm]	Spandrel Height [mm]
1	30	no spandrel
2	30	35
3	30	70
4	50	no spandrel
5	50	35
6	50	70
7	70	no spandrel
8	70	35
9	70	70
10	no cavity	no spandrel
11	no cavity	35
12	no cavity	70

Table 3-2 Overview of SWM experiments.

Additionally, the effects of altering the inter-plate spacing have been studied. Reference to traditional single-skin façade conditions are given in *tests 10, 11 & 12*. Further, the influence of spandrels and spandrel height has been investigated accordingly for the above mentioned scenarios.

3.6 Flow Analysis

In this section, the previously mentioned effects of spandrel- and cavity dimensions will be applied in a holistic manner to illustrate linkage between entrainment flow into the compartment and cavity mass flow. A general mass flow description is given in Figure 3-6 where $\dot{m}_{f,i}$ represents the steady-state salt-water injection into the compartment and $\dot{m}_{f,o}$ the spill out into the cavity. Fresh-water entrainment from the cavity space into the compartment is shown as $\dot{m}_{f,e}$. While the value of $\dot{m}_{f,i}$ is kept constant as an independent parameter of the problem, $\dot{m}_{f,e}$ and $\dot{m}_{f,o}$ are the results of interactions between compartment, spandrel and cavity. Given the limitations of the experimental set-up, $\dot{m}_{f,i}$ could not be varied in a systematic manner, nor the

dimensions of the compartment, nevertheless, the observations presented here do allow to establish the roles of spandrel and cavity dimensions.

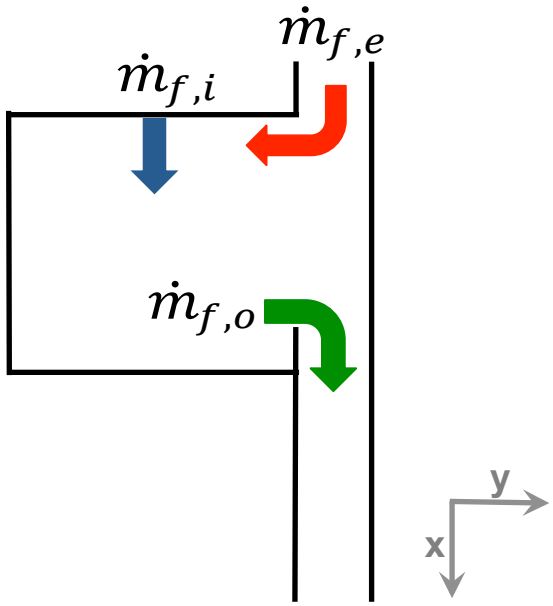

Figure 3-6 Governing mass flows ($\dot{m}_{f,i}$, $\dot{m}_{f,o}$, $\dot{m}_{f,e}$) through compartment and cavity space.

In order to demonstrate spandrel height- and cavity width effects, cavity mass flow rates ($\dot{m}_{f,o}$) have been plotted in Figure 3-7 for different spandrel- and cavity width-dimensions. The corresponding experimental parameters of the tests presented have been illustrated in Table 3-2. The graph shows a dependency of $\dot{m}_{f,o}$ on spandrel height. The introduction of spandrels and their increase in height leads to decreasing mass flow rates within the cavity (*tests 1-9*), as well as in the open cases (*tests 10-12*). An increased spandrel results in a weaker initial momentum of the spill plume, this reduces turbulence and hence fresh-water entrainment into the plume. Therefore, an increase in spandrel height leads to an overall decreasing mass flow entering the cavity.

Reducing the cavity width from 70- to 50 mm has negligible effects on $\dot{m}_{f,o}$, showing almost identical values. A further decrease down to 30 mm however does reduce mass flow due to increased friction losses of $\dot{m}_{f,o}$ at the cavity walls. This behaviour has also been confirmed by [31]. The experimental setup did not allow for

$\dot{m}_{f,e}$ to be measured but can under the law of conservation of mass [46] be assumed to be equal to $\dot{m}_{f,o}$ since $\dot{m}_{f,i}$ is constant.

Removing the outer cavity plate (*tests 10-12*) allows for an unobstructed outflow of $\dot{m}_{f,o}$ into ambient fresh-water. Mass flow increases significantly when no spandrel is in place (test 10) and momentum is the dominant driver of the spill plume. Therefore, cavity widths of 30 – 70 mm obstruct a free $\dot{m}_{f,o}$, hindering spill plume entrainment processes and generally decreasing flow rates. A comparison of pressure-driven $\dot{m}_{f,o}$ (spandrels in place), suggests that cavities generally produce increased flow rates in these cases.

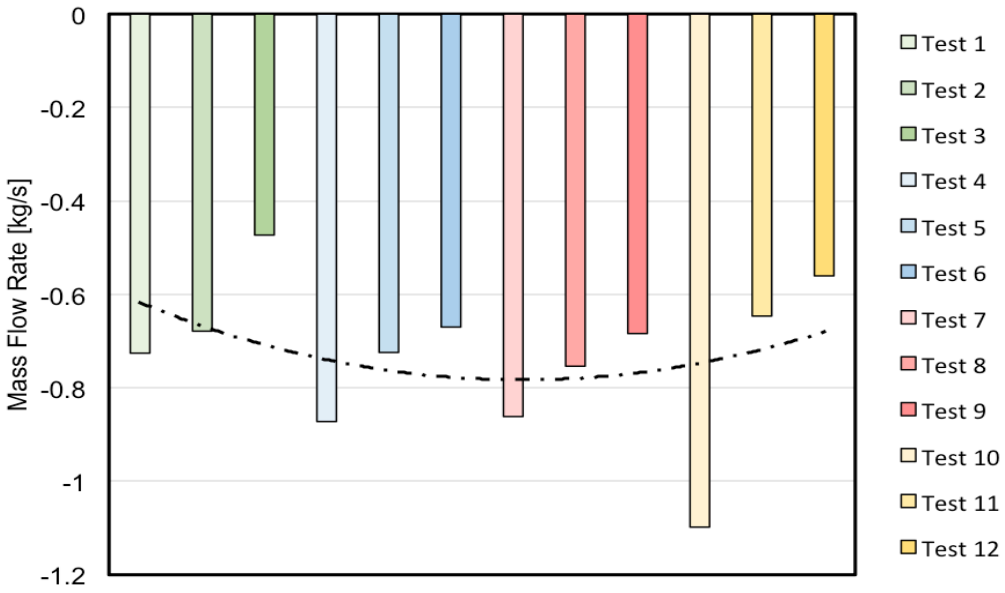

Figure 3-7 Cavity mass flow rates of Tests 1 to 12 (green bars - 30 mm cavity / blue - 50 mm / red - 70 mm / yellow - open / dashed line - 2nd order polynomial trend line for Test 1-12).

An analysis of the dominating impact on changes in cavity mass flow rate is given in Table 3-3. The different test setups are compared to Test 10 which lacks a spandrel and has a single façade only allowing for unobstructed outflow from the compartment. The table does not show precise linkage between cavity width and mass flow rate. Deviations from the reference can however be attributed to spandrel height where generally cases with a 70 mm spandrel (avg. deviation 45,7 %) differ to a larger extent from Test 10 than 35 mm spandrels (avg. deviation 36,2 %) and cases without (avg. deviation 25,4 %). Hence, spandrels can under the presented conditions

be identified to have greater and systematic influence on the cavity mass flow rate than cavity width.

Deviation to Test 10 [%]	Test	Mass Flow Rate [kg/s]	Spandrel Height [mm]	Cavity Width [mm]
56,9 %	Test 3	-0,47	70	0,03
49,0 %	Test 12	-0,56	70	single facade
41,2 %	Test 11	-0,65	35	single facade
39,1 %	Test 6	-0,67	70	0,05
38,3 %	Test 2	-0,68	35	0,03
37,8 %	Test 9	-0,68	70	0,07
34,1 %	Test 5	-0,72	35	0,05
34,0 %	Test 1	-0,73	no spandrel	0,03
31,3 %	Test 8	-0,75	35	0,07
21,6 %	Test 7	-0,86	no spandrel	0,07
20,6 %	Test 4	-0,87	no spandrel	0,05
100 %	Test 10	-1,10	no spandrel	single facade

Table 3-3 Analysis of the influencing factors on mass flow into the cavity space $\dot{m}_{f,o}$ by their deviation from the reference test (Test 10, no spandrel, single facade).

Figure 3-8 presents the vertical locations of the neutral planes (zero net flow) along the compartment vent, marking the boundary between $\dot{m}_{f,o}$ (positive pressure) leaving the compartment and $\dot{m}_{f,e}$ (negative pressure) entering the compartment. The height of the neutral plane is hence induced by pressure differences generated by injection within the compartment and pressure losses within the cavity space.

Although minor, the graph shows slightly decreased neutral plane heights for the narrow 30 mm cavities compared to wider setups. This again can be attributed to decreased $\dot{m}_{f,e}$ into the compartment due to friction losses which in return decreases the plane height because of reduced $\dot{m}_{f,o}$. Increasing the cavity width to 50 mm generally raises the neutral plane due to the previously described processes. However, effects caused by changes in spandrel height become less pronounced compared to the narrower cavity. A further increase of cavity width does not change neutral planes for cases featuring a 35 mm spandrel and without spandrel. Doubling the spandrel height to 70 mm however, leads to a decrease of plane height implying a dependency thereof. Figure 3-7 shows this case as test 9 which features almost

identical $\dot{m}_{f,o}$ compared to test 6 (50 mm spandrel), implying the inconsistency cannot be attributed to a change in mass flow rate.

Figure 3-9 depicts a section (not full height) of the horizontal time-averaged velocities (y-velocities) across the compartment opening, focussing on the different spills into the cavity. The profiles do not allow for a distinct dependency of cavity width on y-velocity to be identified. However, for purely momentum-driven flows (no spandrel) a change in cavity width between 30 and 70 mm does not greatly affect outflow velocities, shown by very similar profiles and values. Increasingly pressure-driven spill plumes (35 & 70 mm spandrels) can be identified by steadily reducing horizontal velocities.

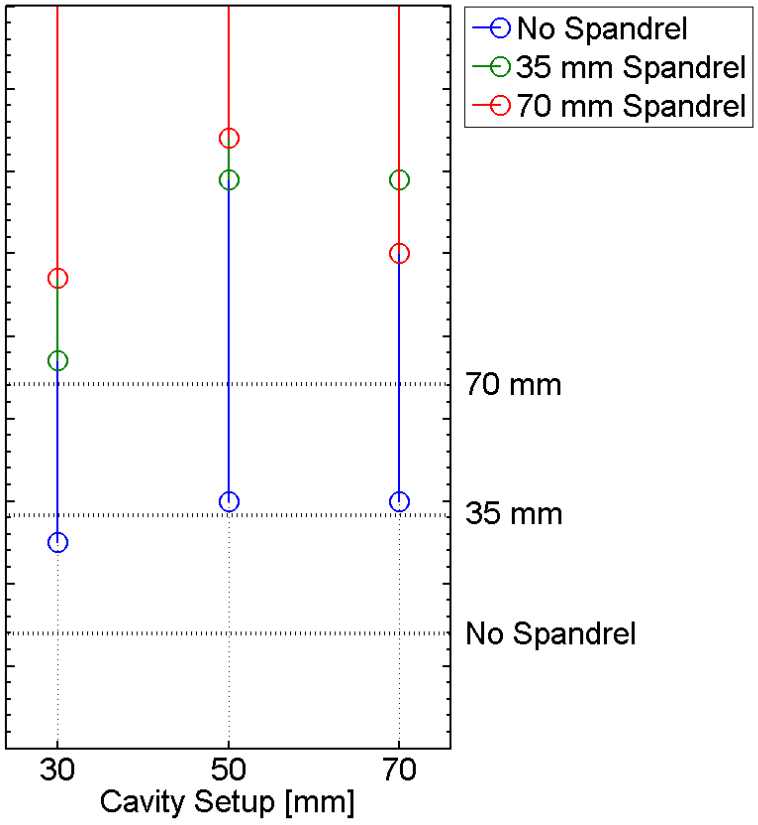

Figure 3-8. Locations of the neutral plane across the compartment opening (between compartment and cavity) of Tests 1 to 9. Dashed lines indicate the positions of the spill edges relative to each other.

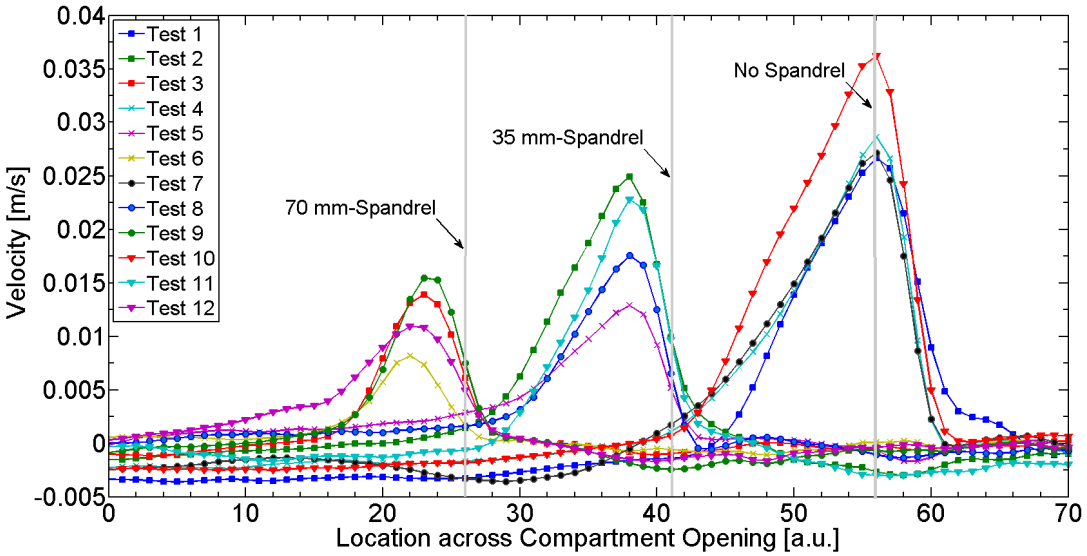

Figure 3-9. Y-velocities across the compartment opening (between compartment and cavity) in Tests 1 to 12.

Linkage between neutral plane height and horizontal velocities at the spill edge is presented in Equation 3-10 and Figure 3-10. Comparing the data presented in Figure 3-8 & Figure 3-9, the following assumptions can be inferred:

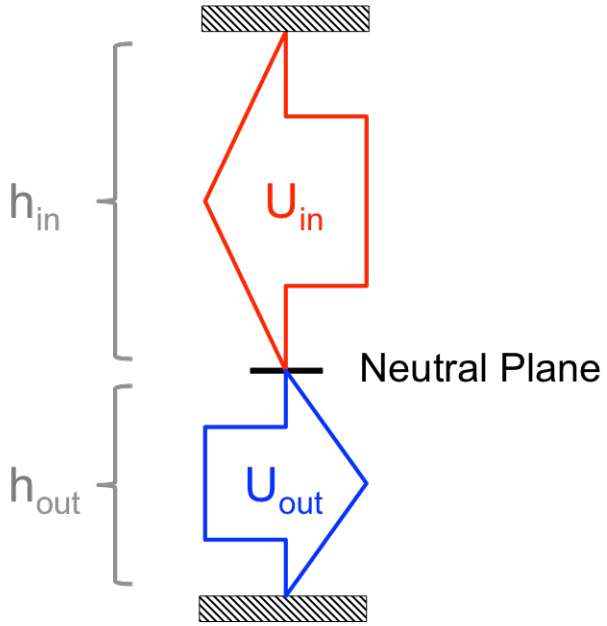

Figure 3-10. Schematic in- and outflow across the compartment opening (densities according to Equation 3-10).

$$U_{out} h_{out} \rho_{out} = U_{in} h_{in} \rho_{in}$$ **Equation 3-10**

In cases where no spandrel is in place, the unobstructed $\dot{m}_{f,o}$ shows high velocities, rel. high water density and low neutral plane heights regardless of changes in cavity width. In return, this leads to an increased inflow height which occurs at decreased velocities.

$$\uparrow U_{out} \downarrow h_{out} \uparrow \rho_{out} = \downarrow U_{in} \uparrow h_{in} \rho_{in}$$ **Equation 3-11**

where,

$\rho_{in} = const.$

A 35 mm spandrel, obstructing $\dot{m}_{f,o}$, reduces horizontal velocities and water density (due to increased turbulent mixing in the volume created by the spandrel) and leads to greatly increased heights of the neutral planes. Accordingly, $\dot{m}_{f,e}$ features increased velocities over decreased inflow heights.

$$\downarrow U_{out} \uparrow h_{out} \downarrow \rho_{out} = \uparrow U_{in} \uparrow h_{in} \rho_{in}$$ **Equation 3-12**

where,

$\rho_{in} = const.$

When a 70 mm spandrel is in place, $\dot{m}_{f,o}$ velocities and water densities decrease further and compared to a 35 mm spandrel, the neutral plane height reduces noticeably. Therefore and compared to a 35 mm spandrel, entrainment velocities decrease and entrainment heights increase. The main impact here can be attributed to the spandrel height.

$$\downarrow\downarrow U_{out} \downarrow h_{out} \downarrow\downarrow \rho_{out} = \downarrow U_{in} \uparrow h_{in} \rho_{in}$$ **Equation 3-13**

where,

$\rho_{in} = const.$

Figure 3-11 shows vertical locations within the cavity from where on fully developed flow behaviour can be identified (interrogation region (a_2), here, Figure 3-3). Flows featuring a spandrel in wider cavities (50- and 70 mm) transition to stabilized behaviour at the same down-flow location, regardless of the cavity width which can be attributed to almost identical $\dot{m}_{f,o}$ as shown in Figure 3-7. Momentum-driven flows (no spandrel) develop sooner with decreasing cavity width which acts as physical constraint, forcing stabilization. In the narrowest cavity (30 mm) the stabilization generally occurs at earlier stages due to decreased flow rates. However, this is not true when a 70 mm spandrel is in place which shows significantly delayed full development. This test (3) also shows the lowest $\dot{m}_{f,o}$ of all cases in Figure 3-7.

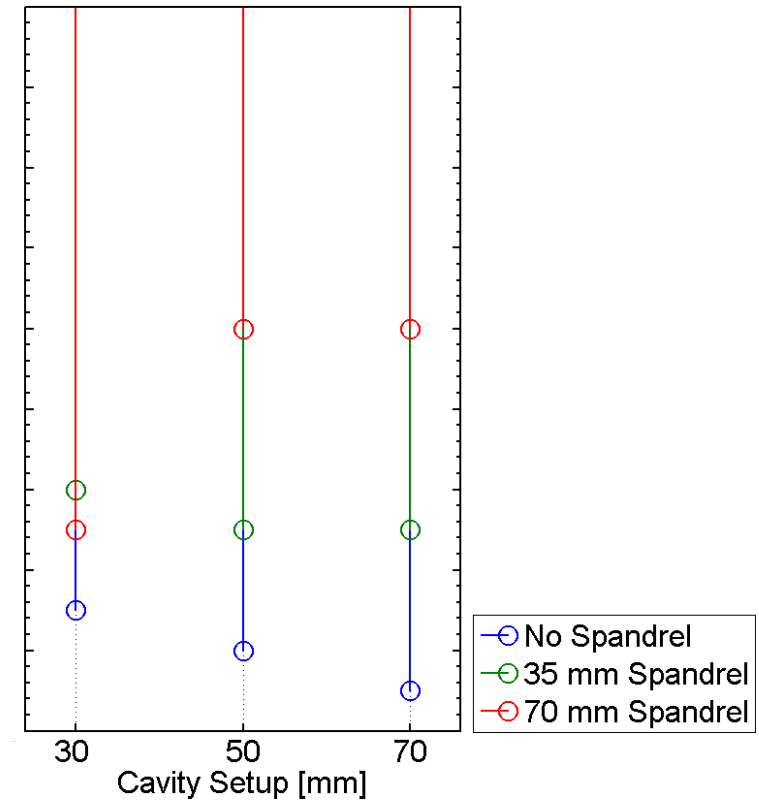

Figure 3-11. Locations of starting fully-developed flow behaviour inside cavities relative to each other (Test 1-9).

In summary, cavity widths affect mass flow rates in the model by decreasing $\dot{m}_{f,o}$ *and* $\dot{m}_{f,e}$ due to friction losses compared to open cases. Respectively, neutral

plane heights decrease when spandrels are in place (effect intensifies with spandrel height) hereby also reducing $\dot{m}_{f,o}$ leaving the injection compartment. In cases where the spill plume is highly momentum-driven, cavity width does not affect horizontal velocities directly at the spill edge, leading to only minor changes in flow development and neutral plane height between various cavity widths.

The introduction of spandrels and their increase in height reduces horizontal spill velocities and $\dot{m}_{f,o}$. Fully developed character of the cavity flow generally establishes earlier with increasing spandrel height.

3.7 The Influence of Spandrels on the Cavity Flow

This section discusses the effects of spandrels and respectively their height when installed between the injection compartment and cavity space. The data presented in the cases to follow is time-averaged, collected at steady-state flow conditions ensuring uniform spill over the spandrel and is spatially averaged over the interrogation region.

Figure 3-12 describes the downstream influence of 35 and 70 mm spandrels in cavities of 30, 50 and 70 mm width on the vertical portion of cavity velocities (y-direction). Each plot also features the corresponding case lacking a spandrel for the purpose of comparison. Velocities where measured across the entire width of each cavity starting from the spill edge into the cavity to the end of the cavity. The bounding plates of the cavity (i.e. inner (compartment side) and outer plate) are located in the following graphs at (x = 0 mm) and (x = 30, 50 & 70 mm).

The 30 mm cavity in part (a) shows close-to fully developed flow character throughout the different setups. Apart from a slight velocity increase close to the outer wall when no spandrel is in place (due to higher momentum retention), the general behaviour of the profiles can be deemed similar in shape and magnitude. However, between inner plate and mid-cavity, both spandrel cases show slightly increased velocities. Velocity profiles peak laterally closer to the inner plate with the presence of a spandrel and increasing height due to changing flow character from momentum driven to pressure driven. The resulting momentum loss enables increased flow velocities close to the inner plate.

In a wider 50 mm cavity (b) predominantly the 70 mm spandrel changes flow structure to a boundary layer driven flow. Less pronounced the same shift occurs when a 35 mm spandrel is in place. Fully developed flow character can be seen when no spandrel has been installed. Again, velocity profiles peak laterally closer to the inner plate in the presence of a spandrel and increasing height.

When increased to a width of 70 mm (c), both spandrel cases show distinct boundary layer behaviour with similar peak velocity values. Peaks in all profiles again move closer to the inner plate in this setup.

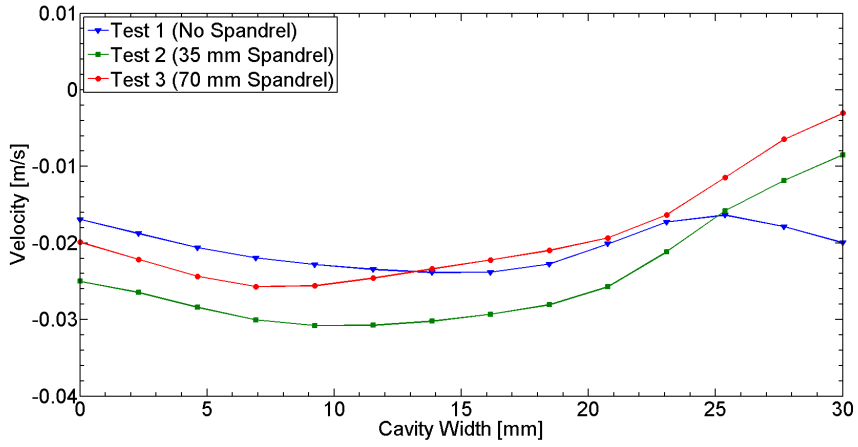

(a)

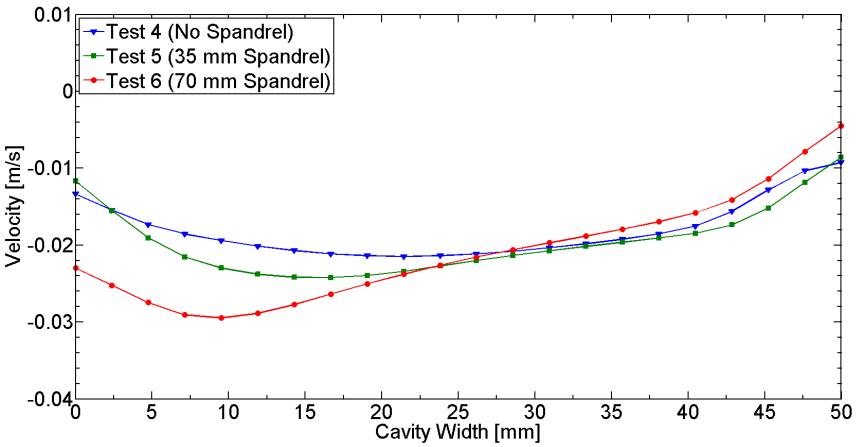

(b)

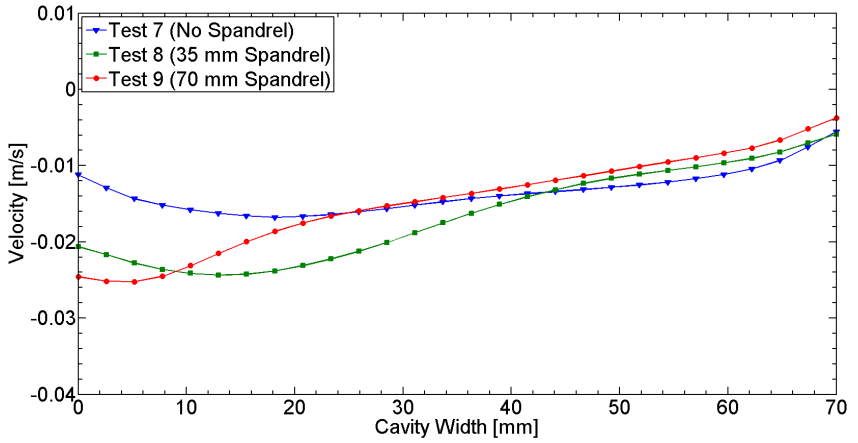

(c)

Figure 3-12. Dependence of vertical cavity flow velocities on spandrels in a 30 mm cavity (a), a 50 mm cavity (b) and a 70 mm cavity (c). Inner façade x = 0, outer façade x = 30/50/70.

For comparison, Figure 3-13 depicts tests where no secondary vertical plate has been installed. As can be expected, flows in all cases show boundary layer character and significantly increased velocities featured when no spandrel is in place. In this setup velocities also peak closer to the inner plate in the presence of spandrels but however, show reduced maximum values.

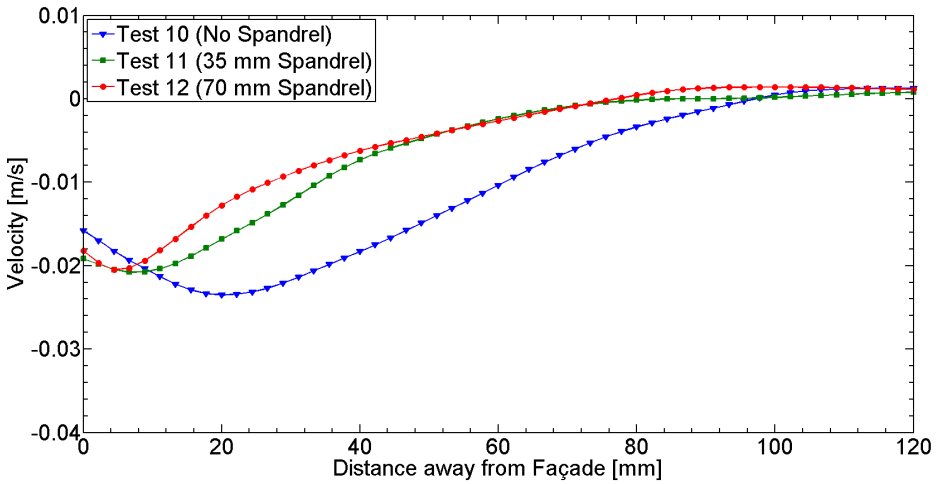

Figure 3-13. Dependence of flow velocities along a single plate on spandrels.

For clarification, Figure 3-14 plots an overview of the peak velocity positions of the above mentioned cases.

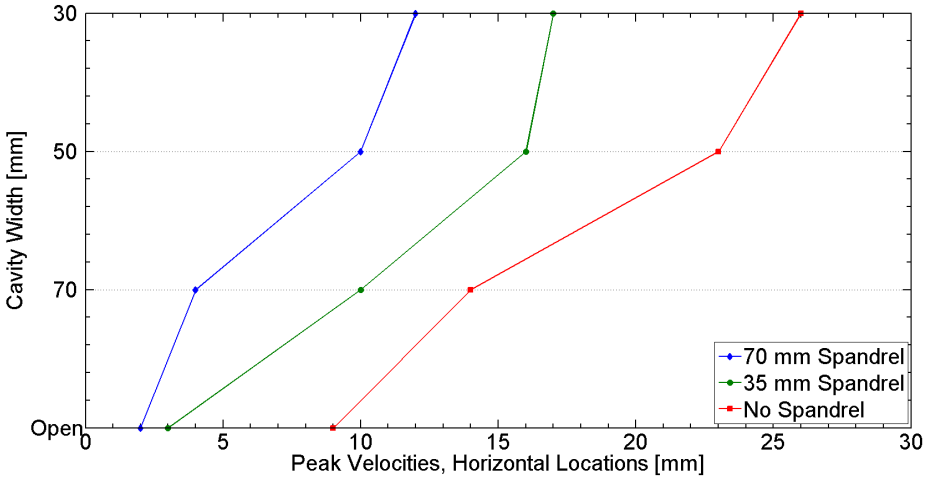

Figure 3-14. Lateral inner-cavity locations of peak velocities in 30- / 50- & 70-mm cavities and a setup featuring no secondary vertical plate (open).

In summary, the presence of spandrels but also their dimensions affect the cavity flow. Velocities along the inner plate rise with the introduction of spandrels and peak

closer towards them with increasing height due to a reduction of horizontal momentum in a progressively pressure driven flow.

3.8 The Influence of Cavity Width

Having discussed the general model flow and pressure- and buoyancy driven components of the velocity field induced by varying spandrel heights in Chapter 3.7, this section investigates the influence of changes in cavity width on the channel flow character. Therefore, time-averaged velocity data across the full cavity height ((a_2) in here, Figure 3-3) has been collected during steady-state flow conditions. Cavity spacing varies between 30 and 70 mm.

Figure 3-15 (a) illustrates profiles of vertical time-averaged velocities of Test 2 (30 mm cavity) and Test 8 (70 mm cavity) featuring a 35 mm spandrel between compartment and cavity space. The graph suggests a close-to-fully developed flow structure in the relatively narrow 30 mm gap with slightly decreasing velocities along the outer plate. Increasing the cavity width to 70 mm however, shows boundary layer behaviour close to the inner plate. Here velocities peak and almost steadily decay across the cavity width to the outer plate. As can be expected, overall profile velocities are higher in the narrower gap due to identical injector flow rates in both cases. A comparison of the maximum velocities along the x-axis show the 70 mm cavity flow peaking closer to the inner plate than the 30 mm setup.

The effects of inter-plate spacing when no spandrel obstructs the outflow into the cavity are displayed in Figure 3-15 (b). Generally, both tests feature smaller velocity gradients between inner and outer plate compared to part (a), where a 35 mm spandrel is in place. Fully developed flow characteristics can be seen in either case with the 30 mm setup showing slightly reduced velocities closer to the outer plate. Again, the narrower cavity features generally higher velocities but in this instance with less pronounced margins between both profiles. The lateral locations of the maximum velocities move further towards the outer plate but again adhere to the previously observed order (70 mm cavity peak closest to inner plate).

The installation of a 70 mm spandrel is shown in Figure 3-15 (c). Alike seen in part (a) the 70 mm gap allows for the distinct formation of a boundary layer governed flow with steadily decaying velocities towards the outer surface.

The 30 mm spacing again features fully developed flow character with similarly declining velocities closer to the outer plate. It is interesting to note that inner plate velocities are highest in the 70 mm case while mid-channel velocities exceed in the narrower 30 mm cavity. Velocities along the outer plates can be deemed equal. Maximum velocity values are almost equal between the two cavities which has not been the case in the previous examples. Both, but especially the lateral location of the peak in the 70 mm cavity, are very close to the inner plate.

A direct comparison of peak velocities in graphs shown in Figure 3-14, and adding cases not featuring a secondary plate, is presented in Figure 3-13. It is interesting to notice that an increase in cavity width results in a shift of peak velocities considerably closer to the inner plate (X = 0). Closest to it are cases where no secondary vertical plate (open) has been installed.

In summary, the cavity affects the time-averaged, steady-state, channel flow by its width dictating whether fully developed- or boundary layer–governed character prevails. A narrow cavity results in a close-to fully developed flow. An increase in width successively leads to boundary-layer governed flow distinctively separating inner from outer plate flow. The presence of a spandrel decreases the distance between inner plate and velocity profile peaks. This effect amplifies with increasing spandrel height.

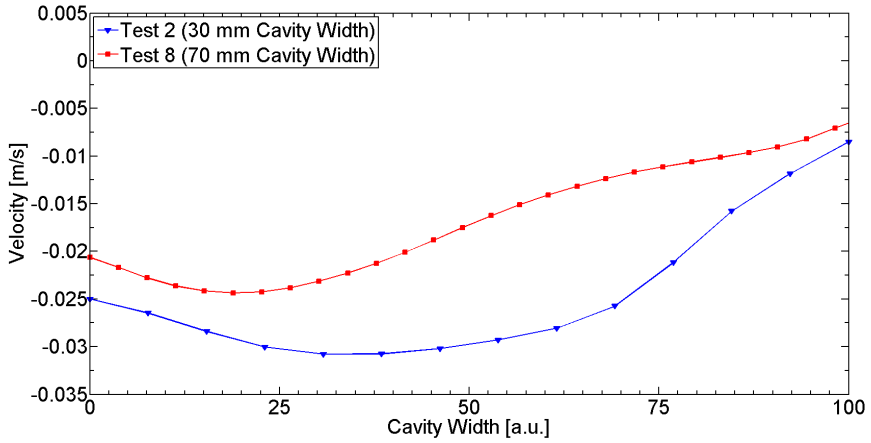

(a)

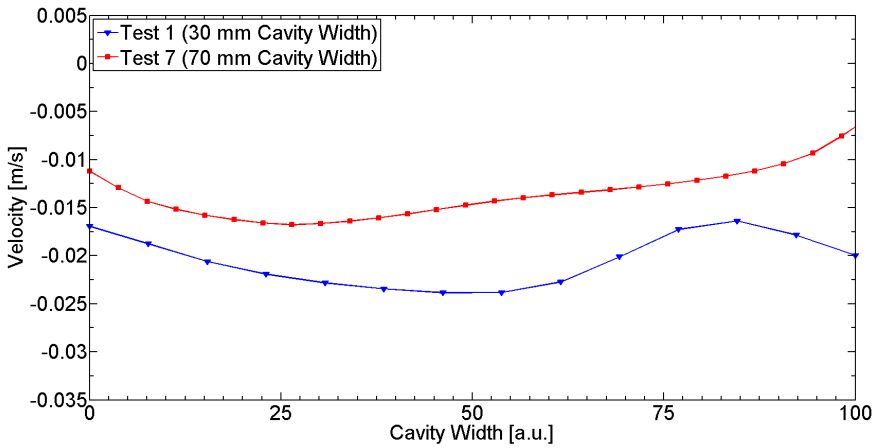

(b)

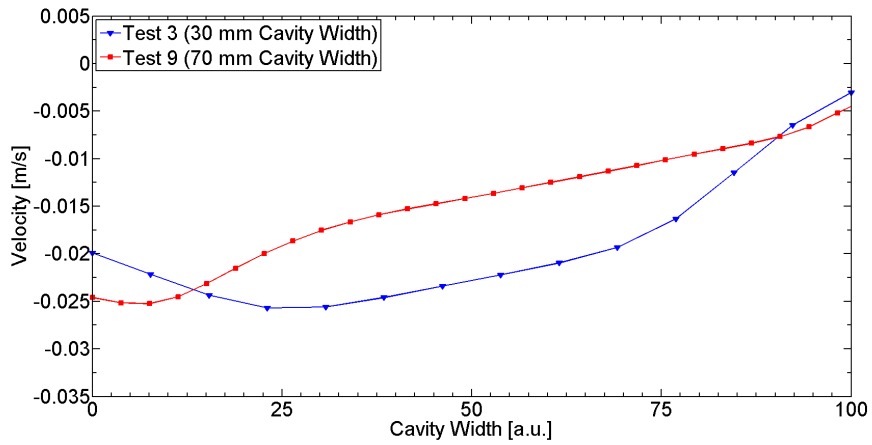

(c)

Figure 3-15. Time-averaged vertical velocity profiles in 30- and 70-mm cavities. (a) 35 mm spandrel; (b) no spandrel; (c) 70 mm spandrel.

3.9 Normalized Velocities

Sections 3.6 to 3.8 aimed to identify flow characteristics in terms of time-averaged velocity profiles which establish under the various different test parameters. In order to achieve relative comparability, these velocities will here be normalized and characteristic length scales and velocities explored to identify the governing mechanisms.

This section will discuss the governing flow phenomena occurring in the façade cavity between inner and outer plate. In general, three flow regimes can be identified, *boundary layer*, *fully developed* and a regime with a plume like structure of the spill between the cavity walls, from here on called *plume regime.*

Jaluria [47] explains, in order to exist, any fluid flow requires a driving mechanism since it is an intrinsic property of fluids to dissipate work. Since in SWM the flow is not forced but natural, its driving force is the buoyancy effect due to gravitational acceleration and density differences between fluid layers.

3.9.1 Boundary Layer Regime

In this regime the thermal boundary layer thickness δ_T is negligibly small in comparison to the plate height H ($\delta_T \ll H$) [47].

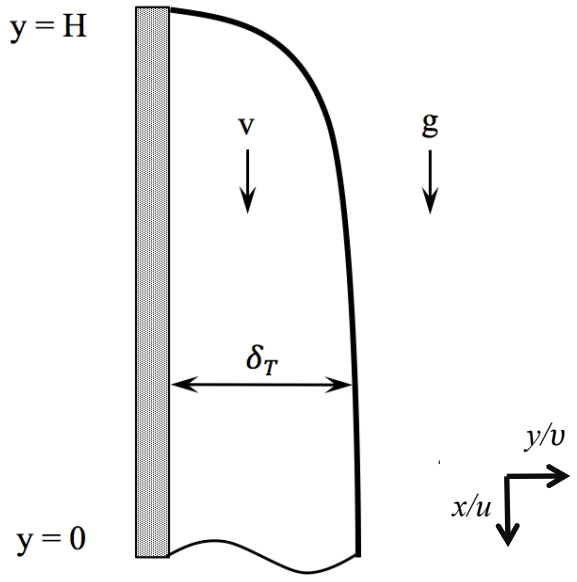

Figure 3-16 Salt-water boundary layer.

The resulting Navier-Stokes equations for steady, two-dimensional flow are:

$$\frac{\partial u}{\partial x} + \frac{\partial v}{\partial y} = 0 \qquad \textbf{Equation 3-14}$$

$$\rho\left(u\frac{\partial u}{\partial x} + v\frac{\partial u}{\partial y}\right) = -\frac{\partial P}{\partial x} + \mu\nabla^2 \qquad \textbf{Equation 3-15}$$

$$\rho\left(u\frac{\partial v}{\partial x} + v\frac{\partial v}{\partial y}\right) = -\frac{\partial P}{\partial y} + \mu\nabla^2 u + \rho g \qquad \textbf{Equation 3-16}$$

$$u\frac{\partial T}{\partial x} + v\frac{\partial T}{\partial y} = \alpha\nabla^2 T \qquad \textbf{Equation 3-17}$$

Since the focus of the analysis is the boundary layer region ($x \sim \delta_T$, $y \sim H, \delta_T \ll H$) the governing equations (Equation 3-14 to Equation 3- 17) reduce to simpler forms. From the x-momentum equation (Equation 3-15) it becomes clear that the pressure in the boundary layer is a function of longitudinal position only (Equation 3-18) [47].

$$\frac{\partial P}{\partial y} = \frac{dP}{dy} = \frac{dP_\infty}{dy} \qquad \textbf{Equation 3-18}$$

Boundary layer equations for momentum and energy are respectively

$$\rho\left(u\frac{\partial v}{\partial x} + v\frac{\partial v}{\partial y}\right) = -\frac{dP_\infty}{dy} + \mu\frac{\partial^2 v}{\partial x^2} + \rho g \qquad \textbf{Equation 3-19}$$

$$u\frac{\partial T}{\partial x} + v\frac{\partial T}{\partial y} = \alpha\frac{\partial^2 T}{\partial x^2} \qquad \textbf{Equation 3-20}$$

Keeping in mind that dP_∞ / dy is the hydrostatic pressure gradient with density ρ_∞, $dP_\infty / dy = \rho_\infty g$, the resulting momentum equation is

$$\rho\left(u\frac{\partial v}{\partial x}+v\frac{\partial v}{\partial y}\right)=\mu\frac{\partial^2 v}{\partial x^2}-(\rho_\infty-\rho)g \qquad \textbf{Equation 3-21}$$

In contrast to real fires, in SWM the fluid flow is not driven by the density field $\rho(x,y)$ generated by the temperature field T (x,y) but solely by density variations. Applying the ideal gas model the densities in- and outside the boundary layer behave as follows [47]

$$\rho=\frac{P_\infty/_R}{T} \qquad \textbf{Equation 3-22}$$

$$\rho_\infty=\frac{P_\infty/_R}{T_\infty} \qquad \textbf{Equation 3-23}$$

$$\rho-\rho_\infty=\rho\left(1-\frac{T}{T_\infty}\right) \qquad \textbf{Equation 3-24}$$

Rearranging this expression and setting the limit $(T-T_\infty)\ll T_\infty$ yields

$$\rho=\rho_\infty[1-\beta(T-T_\infty)+\cdots] \qquad \textbf{Equation 3-25}$$

where the density decreases below ρ_∞ when the local temperature increases above the surrounding fluid temperature T_∞. Here β is the volume expansion coefficient at a constant pressure [47]

$$\beta=-\frac{1}{\rho}\left(\frac{\partial\rho}{\partial T}\right)_P \qquad \textbf{Equation 3-26}$$

Applying the Boussinesq approximation in the boundary layer equations (the dimensionless product $\beta(T-T_\infty)$ is considerably smaller than unity), the leading body force term becomes $\rho_\infty\beta g(T-T_\infty)$. The linkage between temperature- and

flow field is shown in the Boussinesq-approximated momentum equation (Equation 3-27) [47].

$$u\frac{\partial v}{\partial x} + v\frac{\partial v}{\partial y} = v\frac{\partial^2 v}{\partial x^2} + g\beta(T - T_\infty) \qquad \textbf{Equation 3-27}$$

3.9.2 Vertical Channel Flow

The interaction between natural convection boundary layers forming between two parallel plates will be discussed in this section (Figure 1-1). Generally, the flow pattern depends on the boundary layer thickness. If the scale is much smaller than the inter-plate spacing *D*, the flow driving along one wall is mainly unaffected by the presence of the opposite wall. In contrast, if the boundary layer thickness increases to a comparable size similar to D, the two plate jets merge into a single buoyant stream.

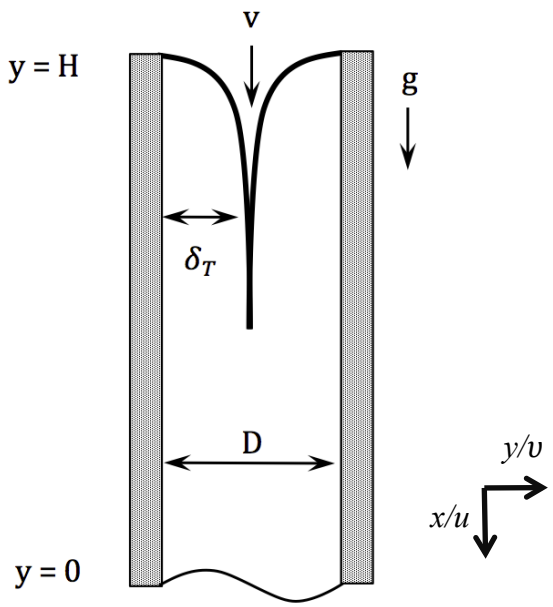

Figure 3-17 Salt-water channel flow.

Fully developed flow establishes from the mass continuity equation (Equation 3-14) under the assumption that the vertical channel is sufficiently long so that the *u* scale becomes small [47].

$$u = 0 \; and \; \frac{\partial v}{\partial y} = 0 \qquad \textbf{Equation 3-28}$$

The pressure in the fully developed flow is a function of the channel height y and ρ_∞ since the channel ends are being left open.

$$\frac{\partial P}{\partial y} = \frac{dP}{dy} = +\rho_\infty g \qquad \textbf{Equation 3-29}$$

The momentum equation in the y direction combined with the concepts presented in Equation 3-28 and Equation 3-29 and applying the Boussinesq approximation leads to the following general and simplified equation.

$$\frac{d^2 v}{dx^2} = +\frac{g\beta}{v}(T - T_\infty) \qquad \textbf{Equation 3-30}$$

In SWM this expression has to be given in terms of density, not temperature, which relates via the ideal gas model as follows [47]:

$$PV = mRT \qquad \textbf{Equation 3-31}$$

$$P = \rho RT$$

$$P_\infty = \rho RT_\infty$$

$$\rho_\infty = \frac{P_\infty}{RT_\infty}$$

$$\rho = \frac{P_\infty}{RT}$$

$$dP = (\rho_\infty - \rho)gy \qquad \textbf{Equation 3-32}$$

$$\frac{\partial P}{\partial y} = (\rho_\infty - \rho)g$$

$$\frac{\mu}{\rho_\infty}\frac{\partial^2 v}{\partial y^2} = \left(\frac{\rho_\infty - \rho_0}{\rho_\infty}\right) g \qquad \textbf{Equation 3-33}$$

$$\frac{\partial^2 v}{\partial y^2} = \left(\frac{\rho_\infty - \rho_0}{\nu \rho_\infty}\right) g$$

Introducing the Rayleigh number and once again applying the Boussinesq approximation leads to the characteristic velocity $V_{c,fd}$ for fully developed flow [47].

$$Ra = Gr \cdot Pr \qquad \textbf{Equation 3-34}$$

$$Ra_D = \frac{g\beta D^3 (T_0 - T_\infty)}{\propto \nu} \qquad \textbf{Equation 3-35}$$

$$\frac{\rho_\infty - \rho_0}{\rho_\infty} = \beta (T_0 - T_\infty) \qquad \textbf{Equation 3-36}$$

$$\frac{\rho_\infty - \rho_0}{\rho_\infty} = \frac{\rho_{freshwater} - \rho_{saltwater}}{\rho_{freshwater}} \qquad \textbf{Equation 3-37}$$

$$V_{c,fd} = \frac{\alpha}{8D} Ra_D = \frac{gD^2(\rho_\infty - \rho_0)}{8\nu\rho_\infty} \qquad \textbf{Equation 3-38}$$

The salt-water density ρ_0 of the spill flow into the cavity space can be calculated using the correlation in Equation 3-39 where H is the height of the spill flow over the spandrel edge, W the width of the compartment opening and $\bar{u}$ the average flow velocity inside the cavity over the full height.

$$\bar{\rho} = \rho_W + \frac{\dot{m}_{in}}{\bar{u} H W} \qquad \textbf{Equation 3-39}$$

$$\mu \frac{\partial^2 v}{\partial x^2} = (\rho_\infty - \rho) g \qquad \textbf{Equation 3-40}$$

In boundary layer flow the characteristic velocity $V_{c,bl}$ must be modified to [47]

$$V_{c,bl} = \frac{\alpha}{H} Ra_H^{\frac{1}{2}} = \frac{gH^3(\rho_\infty - \rho_0)}{\rho_\infty} \qquad \textbf{Equation 3-41}$$

3.10 Preliminary Conclusions

Chapter 3 presents the principles of the SWM technique along with a dimensionless analysis of the governing equations of fire-induced and salt-water flow with corresponding dimensionless parameters. A detailed description of the experimental setup, parameters and data acquisition is given upon the general flow analysis and the influence of spandrels and cavity width on the flow development. Here, the main conclusions are:

- Cavity widths affect mass flow rates in the model by decreasing $\dot{m}_{f,o}$ *and* $\dot{m}_{f,e}$ due to friction losses compared to open cases
- In cases where the spill plume is highly momentum-driven, cavity width does not affect horizontal velocities directly at the spill edge, leading to only minor changes in flow development and neutral plane height between various cavity widths.
- Spandrel height has a larger influence on $\dot{m}_{f,o}$ than cavity width
- The introduction of spandrels and their increase in height reduces horizontal spill velocities and $\dot{m}_{f,o}$
- Fully developed character of the cavity flow generally establishes earlier with increasing spandrel height
- The presence of spandrels but also their dimensions affect the cavity flow
- Velocities along the inner plate rise with the introduction of spandrels and peak closer towards them with increasing height due to a reduction of horizontal momentum in a progressively pressure driven flow
- Cavities affect the flow by its width dictating whether fully developed- or boundary layer–governed character prevails

Lastly, a general description of normalisation of the flow velocities is explored.

4 Large-Scale Fire Tests

The second phase of the experimental analysis will here be presented in the form of large-scale fire tests performed under the umbrella of the *Edinburgh Travelling Fire Tests* (ETFT) at *the Building Research Establishment* (BRE), Watford in 2013. These tests have been conducted as part of the *Real Fires for the Safe Design of Tall Buildings* project and aim to help understand the governing fire dynamics in non-compartmented spaces commonly to be found in open-plan floor design for tall buildings. Independent from the main aim of the ETFT programme, the author implemented a series of façade experiments within these tests which will investigate and compare fire-induced flow dynamics of single- and double skin façades.

4.1 General Setup of the Experiments

The main compartment features inner dimensions of 17.80 m (length), 4.90 m (depth) and 2.00 m (height) as illustrated in Figure 4-1 (a). The structure has been raised above ground by 1.00 m for easy accessibility and the top section of the open front face has been blocked by a spandrel of 0.50 m height, reducing the overall opening height to 1.50 m. The front is built of a total of 15 openings each 1.10 m wide.

Neglecting the compartments initial role within the ETFT, its main purpose in the herein presented façade experiments is to act as a heat source, providing a flow of hot gases at steady-state via 12 gas burners. A high density grid of cameras and sensors in and outside the compartment measures temperature, heat flux, pressure, smoke density and -species.

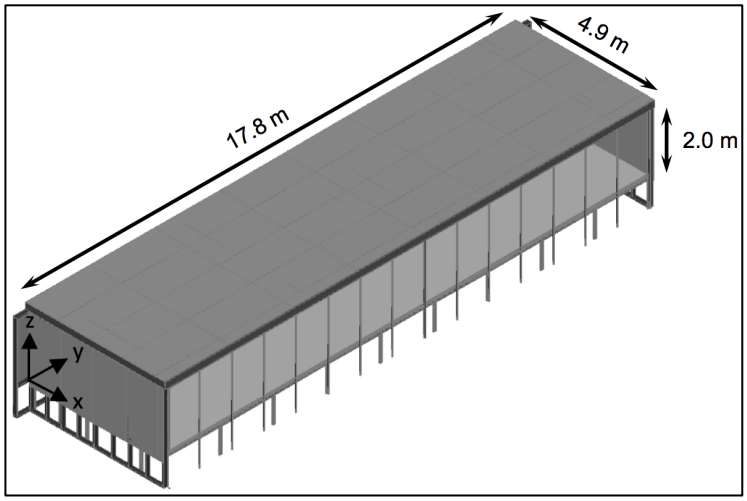

(a)

(b)

Figure 4-1. (a) ETFT compartment sketch (excl. spandrels) and inner dimensions, (b) photograph during testing (incl. spandrels) [48].

4.1.1 Setup of the Façade Experiment

The façade installation is in total 3.60 m wide and 3.30 m high and features a set of three experiments as shown in Figure 4-20 (a) which aim to mimic two DSFs with cavity widths of 0.40 and 0.15 m, and a single façade for comparison. Inner and outer faces of the façades have been constructed from a combination of plaster board on timber framing (top sections) and insulation material (mineral wool) encased in a

metal frame in the lower sections to better withstand the increased heat impact closer to the compartment opening. The assembly was suspended off of the compartment roof by 50 x 50 mm square steel tubing. The sides of the DSFs have deliberately been left open to allow unconfined flow to establish.

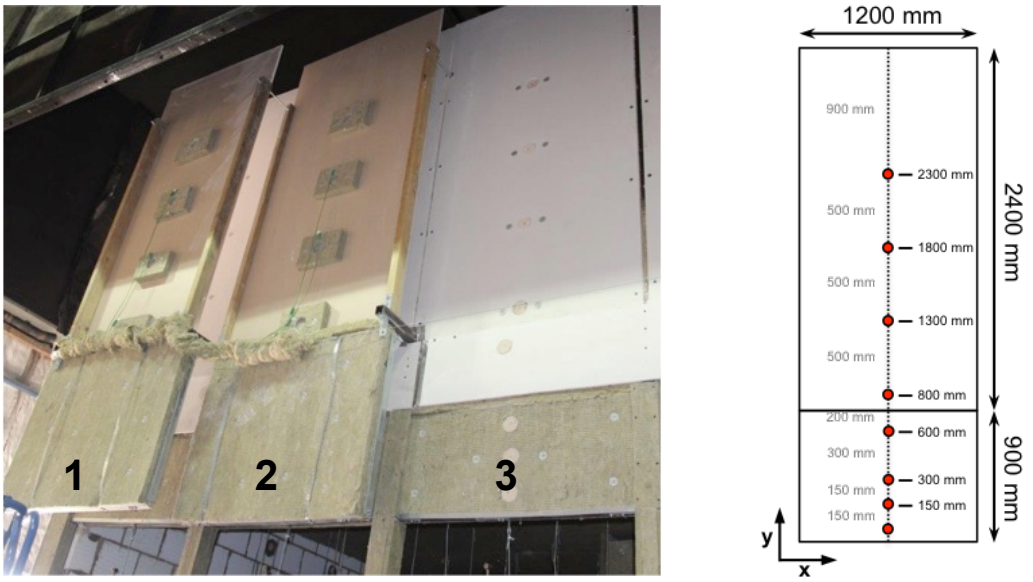

(a) (b)

Figure 4-2. (a) Large-scale DSF setup during testing, (1) 0.40 m cavity, (2) 0.15 m cavity, (3) single façade. (b) Distribution of TSCs (red dots) along inner and outer face of the single- and DSF. Light grey measurements depict spacing between TSC's, measurements in black show their absolute location along the y-axis.

4.1.2 Instrumentation

Custom designed Thin Skin Calorimeters (TSCs) described in [48] have been used to measure incident radiant and convective heat flux to all faces of the façade system. Each skin has been equipped with eight TSC's, from here on called heat flux gauges named HFG-1 to 8 (bottom to top). The gauges are made out of a 10 mm, 0.5 mm thick steel plate with a KX-Type Thermocouple fixed to the rear face. The assembly was then embedded in a 80 mm diameter, 50 mm deep Ceraboard disk which has been mounted flush to the flow facing side of each skin.

Figure 4-2 (b) illustrates their vertical distribution along the centreline of each face. Spacing between single gauges increases from 150 mm (bottom end) up to 500 mm

(top end) to achieve higher accuracy within the immediate area of spill plume impingement. A lower resolution grid has been applied further upstream where a more even flow profile is to be expected. Slightly inconsistent spacing between HFGs-3, 4 & 5 was due to unavoidable experimental constraints.

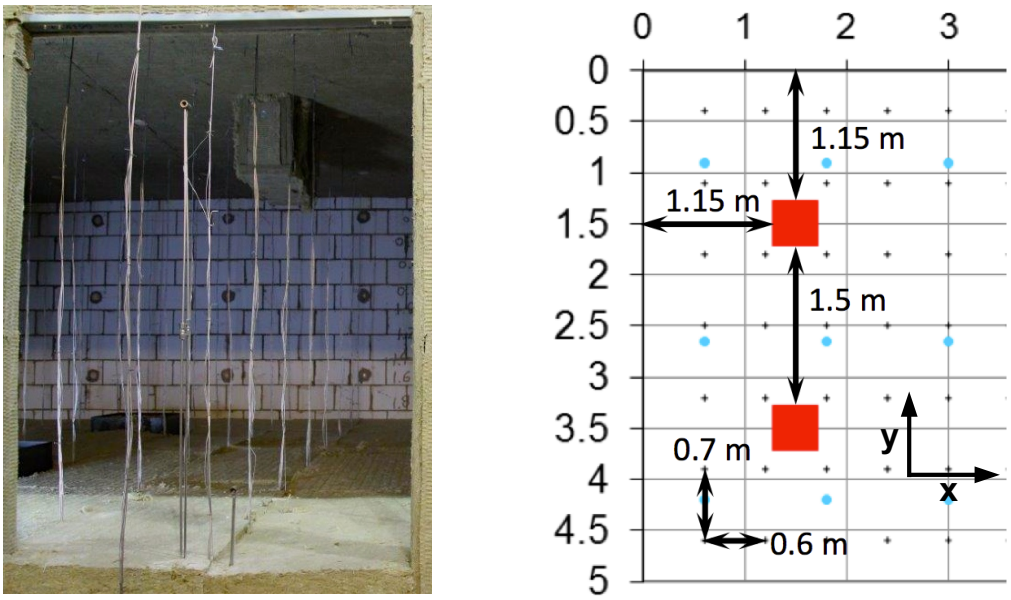

(a) (b)

Figure 4-3. (a) Row of thermocouple trees leading towards each of the 15 compartment openings, (b) excerpt plot and spatial distribution of thermocouple trees (black dots), floor / ceiling heat flux gauges (blue dots), and gas burners (red squares) corresponding to the façade test arrangement illustrated in Figure 4-2 (a). The compartment openings are located along y = 5.

Monitoring conditions inside the compartment has been achieved by a row of seven thermocouple (TC) trees leading towards each opening and each holding eight K-Type TCs, evenly distributed over the full room height at 0.30, 0.60, 0.90, 1.20, 1.40, 1.60, 1.80, and 1.95 m. An additional TC tree has been added within the very compartment opening as can be seen in Figure 4-3 (a) and features TCs at 0.18, 0.43, 0.68, 0.93, and 1.18 m height [48].

4.2 Flow Analysis

A general description of the general flow pattern is given in Figure 4-4. Contrary to the SWM experiments, where the buoyant flow is created “artificially”, two rows of

six gas burners produce hot gas plumes in the large-scale experiments ($\dot{m}_{f,i}$). Upon creation of a sufficiently deep hot gas layer, the spill plume ($\dot{m}_{f,o}$) exits the compartment and enters the cavity space (respectively, impinges along the single façade). The open front of the fire compartment serves as a vent where replacement air entrains ($\dot{m}_{f,e}$).

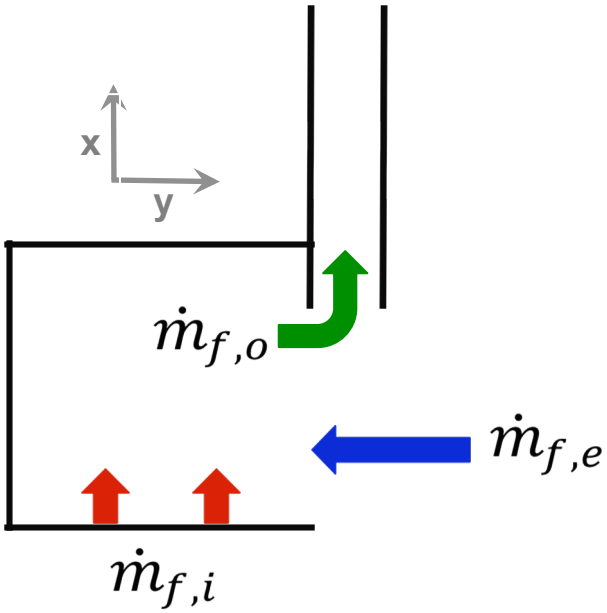

Figure 4-4. General flow through fire compartment and façade of the large-scale experiment.

Within the ETFT framework, façade experiment relevant data has been taken from Test 1, with its parameters shown in Table 4-1. After all gas burners have been ignited, a slow HRR ramp up from 50%, 74% to 99% output has been initiated and held at this level for 5.5 min. This was followed by a slightly decreasing HRR until shut off after 1490 s [48].

A temperature plot of Façade 3 (Figure 4-5) exemplifies the general fire conditions provided by the burners inside the compartment. The HFGs 1-8 correspond to the vertical arrangement shown in Figure 4-2 (b). The data used in the here presented analysis has been collected between event (e) & (f) in Figure 4-5 as this can be identified to be the most steady state like period during this experiment.

The interior compartment temperature distributions and conditions along each median plan of the three façade tests is illustrated in Figure 4-6. The plots depict

constant averaged temperatures of 240 °C at the spill (i.e. spandrel) locations throughout the tests between events (e) and (f). This allows for relative comparability of the thermal spill plume conditions at each opening.

EVENT	Time from Ignition [s]	HRR [kW]	Steady-State [min]
Start Lighting Pilots	-790		
All Burners ON	0		
50% HRR (for ~ 4.5 min)	44	1236	4,57
Begin HRR Increase	318		
74% HRR (for ~ 3.7 min)	370	1853	3,72
Begin HRR Increase	593		
99% HRR (for ~ 5.5 min)	720	2474	5,55
Begin HRR Decrease	1053		
88% HRR (for ~ 3.5 min)	1120	2209	3,50
Begin HRR Decrease	1330		
86% HRR (for ~ 2.3 min)	1350	2153	2,33
Gas OFF	1490		

Table 4-1 Gas burner settings during the façade experiment (ETFT Test 1) [48].

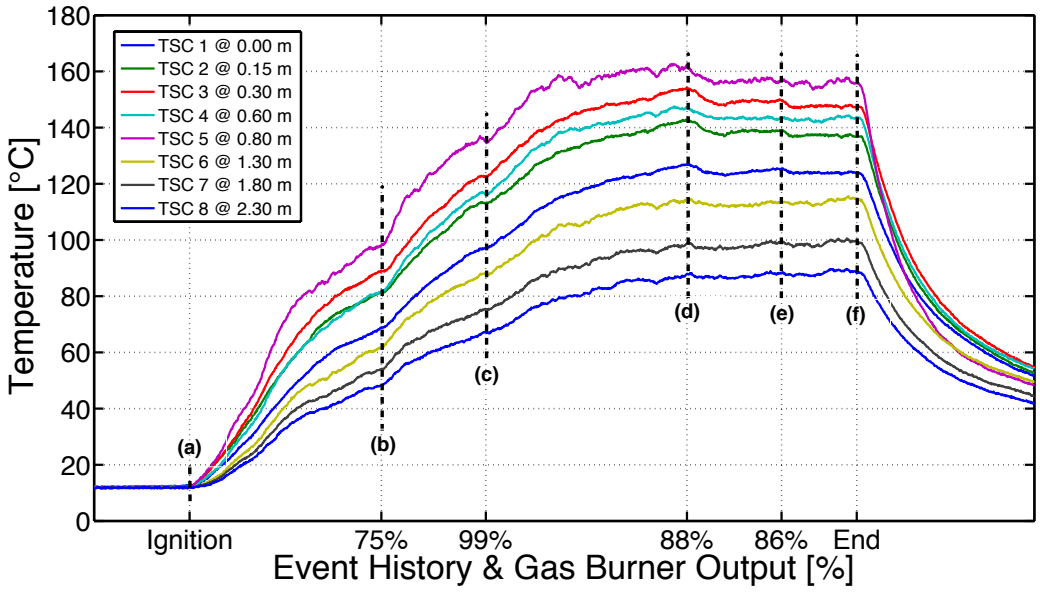

Figure 4-5 Raw, unconverted temperature data of the HFGs in facade experiment 3 (single facade) linked to the sequence of events.

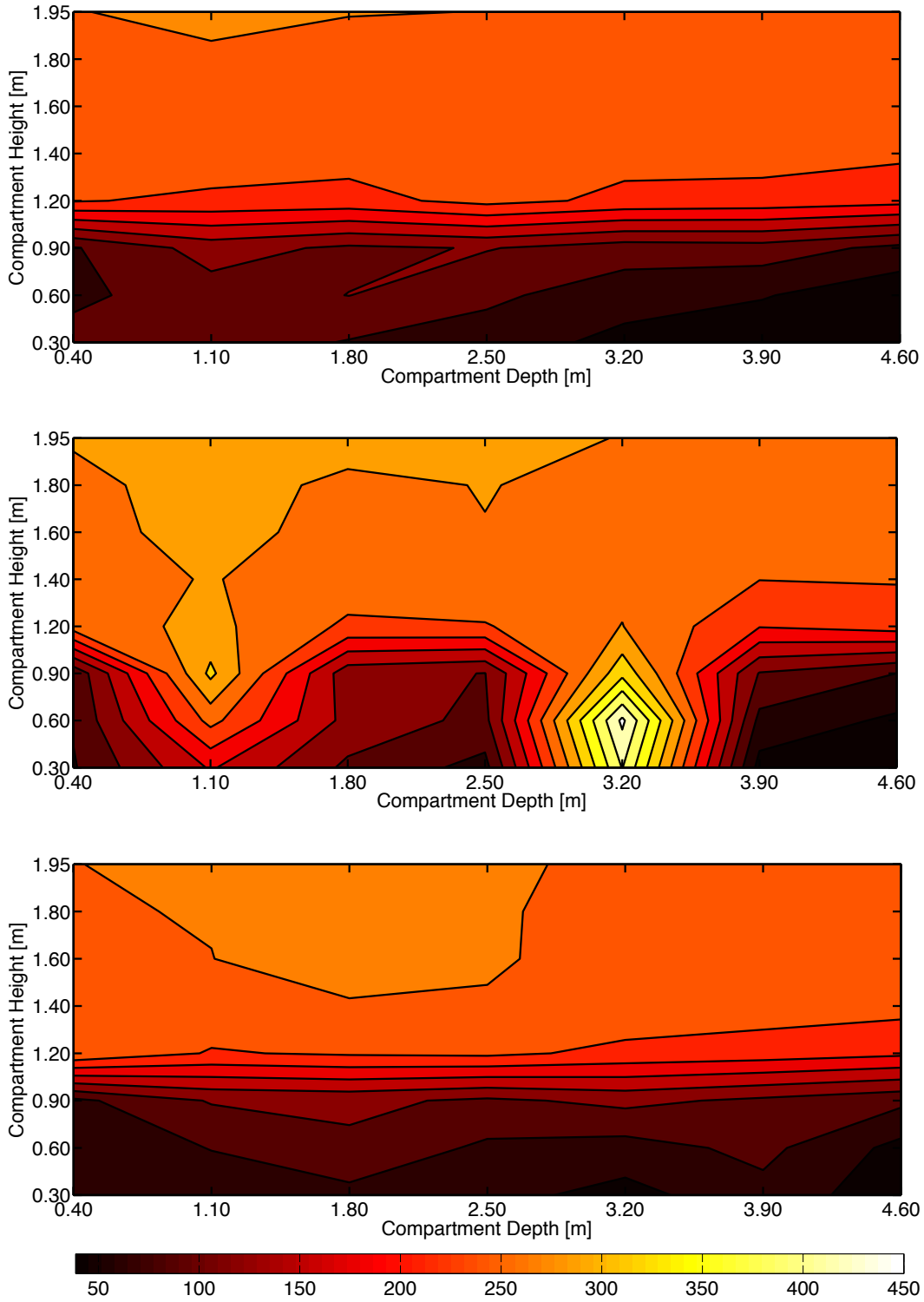

Figure 4-6 Contour plots of the interior compartment temperatures [°C] at centre line of each opening corresponding to Experiment 1, 2 and 3 (top to bottom). Spandrel location is at x = 4.60 m, y = 1.50 to 1.95 m.

4.3 The Effects of Cavity Width

Similar to Chapter 3.8 in the SWM experiments, the influence of a DSF and changes in cavity width, will here be investigated under real fire conditions and on a large-scale. The data used in all tests has been time-averaged over a period of steady-state flow as explained in Chapter 4.2.

For ease of understanding, the flow will first be described using the single façade setup of experiment 3 illustrated in Figure 4-7. As already explained in Figure 4-2 (b), the spacing between HFGs is not consistent over the height of the façade experiment to accommodate the need for increased resolution in the lower section of the test where the initial flow establishment occurs. This inconsistency has been carried to the presented plots to follow, and explains the uneven distribution of tick marks on the y-axis.

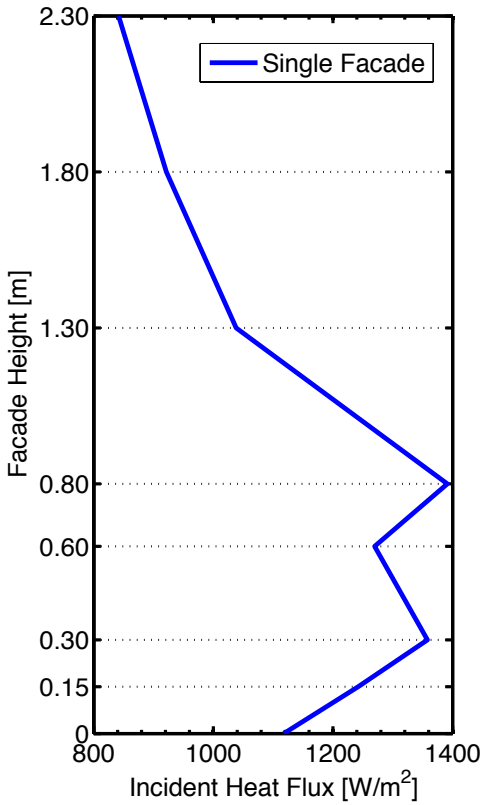

Figure 4-7 Incident heat flux distribution along Façade 3 (single façade).

Upon exiting the fire compartment, the hot gas flow impinges on the façade skin and applies a height-dependent heat flux (Figure 4-7). The plot suggests increased values

in the lower section of the façade up until 0.80 m height where the HF reaches its maximum of 1.4 kW. A slight value drop at 0.60 m above the opening edge might be the result of the *Coanda Effect*. Beyond 0.80 m values drop steadily to a minimum of 0.85 kW at 2.30 m.

In Experiment 1, a secondary façade has been placed at an 0.40 m offset away from the inner skin, creating a void open to all four sides. The hot gas flow entering the cavity results in HF impacting on both inner and outer face and is displayed in Figure 4-8 (a).

Similar to the single façade in Experiment 3 and with only slightly reduced overall HF values (and no localised drop due to the *Coanda Effect*), the incident on the inner façade is bow-shaped in the lower section of the experiment. The peak HF is measured to be at y = 0.30 m and reduced by 0.1 kW in comparison to the single façade. The descent from there on towards the upper end is steady to about 0.85 kW.

In contrast, the impact onto the outer face up to 0.80 m height can be approximated to be the inverse of the inner skin by showing slightly lower overall HFs. This illustrates that immediately after entering the cavity, the flow impinges predominantly on the outer face due to the retaining horizontal momentum of the spill plume. However, further upstream the flow direction reverses back towards the inner skin which becomes evident by increasing HF values and decreasing values at the outer face. Declining HF continues to show in the upper section of the cavity.

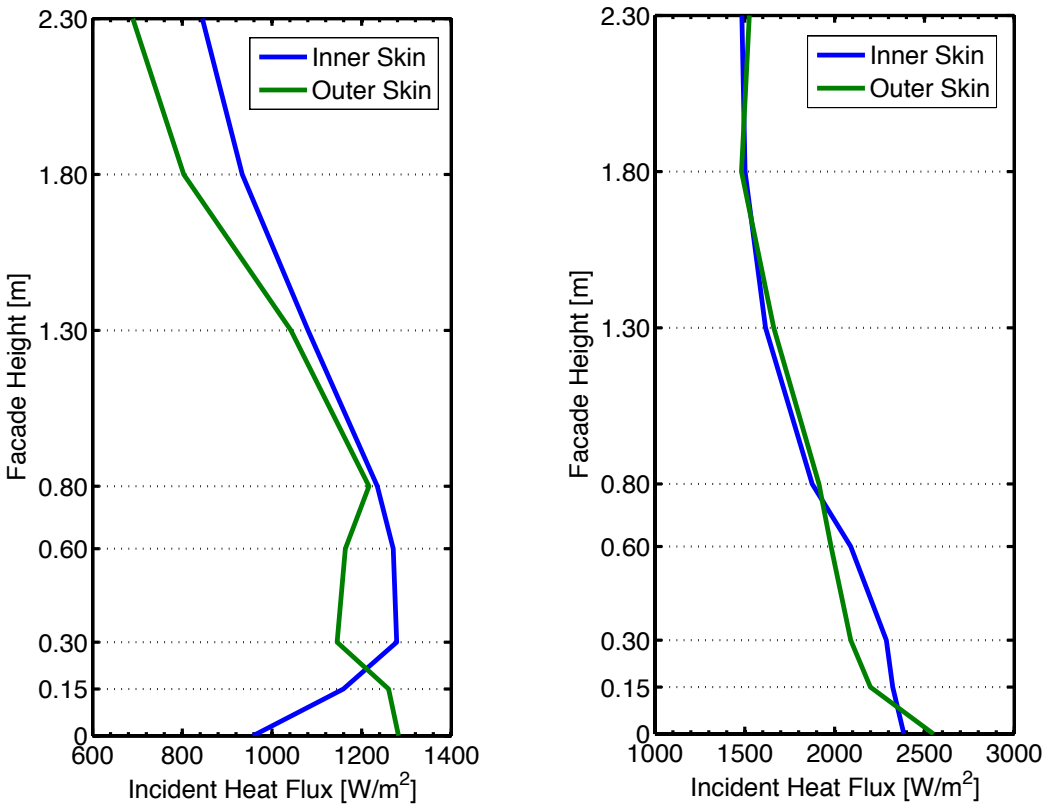

Figure 4-8 Incident heat flux distribution along inner and outer face of the DSF in Test 1 (0.40 m cavity) (a) and Test 2 (0.15 m cavity) (b).

In General, the addition of a second skin at an offset of 0.4 m, reduced the peak HF on the inner skin by ca. 7 % whilst lowering its vertical location by ca. 22 % (in comparison to Experiment 3, single skin setup).

In Experiment 2, the cavity width has been set to 0.15 m. This narrow setup led to overshooting of parts of the combustion gases beyond the cavity due to the large retaining momentum of the gas flow. This lost volume did not contribute to the flow inside the cavity and it can be assumed that temperatures on both faces would have been amplified.

It can be seen that, apart from minor variations, HFs to both faces are of similar magnitude and distribution. This setup forces inner and outer face HFs to peak at the inlet of the cavity. From there on the decay is steady and comparable, above 0.80 m

height even identical from where on the cavity flow seems to have merged completely.

Comparing HFs on the inner skin in Experiment 1 and 2, the narrower cavity shows a 45 % higher HF peak of 2.4 kW. Its vertical location drops by 13 %. Heat flux incident on the outer panes of Test 1 and 2 indicate an increase by approximately 1 kW (48 %) in case of the narrower cavity.

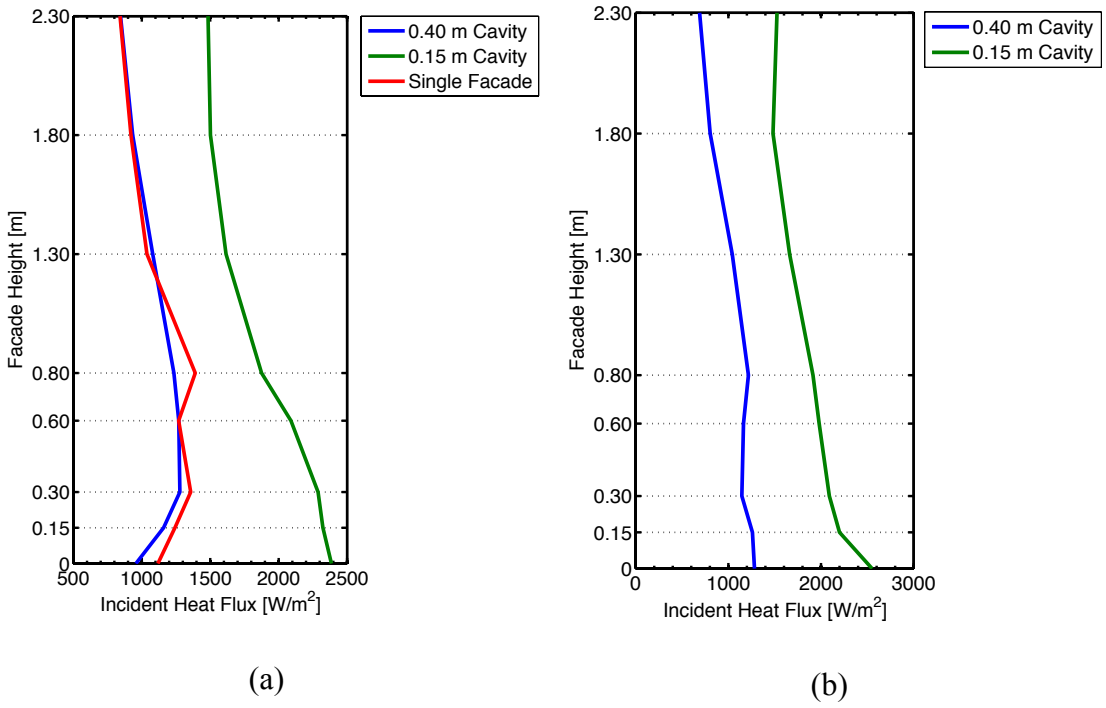

Figure 4-9. Incident heat flux distribution along inner (a) and outer façade (b) in Tests 1, 2 & 3.

4.4 Preliminary Conclusions

In summary, DSFs and changes in cavity width directly influence the incident heat flux on the inner and outer façade (Figure 4-9).

- A wider DSF of 0.40 m width slightly reduced the peak HF impact along with lowering its vertical location when compared to the single skin setup.
- A narrower cavity of 0.15 m width drastically increased the total HF on the inner and outer skin when compared to the wider cavity of 0.40 m and the single façade.
- In narrow cavities the hot gas flow develops early into one well-mixed cavity flow.

- In wider cavities HF impact to inner and outer pane differs in magnitude and distribution.
- Considering the impact to the inner façade above 1.3 m height (i.e. the storey above the fire impacted compartment in a real building), only the narrower DSF shows significantly higher HFs possibly posing a fire risk. At this height single façade and wider DSF show almost identical conditions.
- Not featuring an open outer façade skin, as has been chosen here due to constraints of the main series of experiments (ETFT), can possibly reduce the entrainment flow into the compartment which might have effects on the resulting cavity flow. If at all, this will increasingly influence narrow cavities over wider setups.

It can be inferred that there is a critical cavity width at which the cavity flow transitions from a boundary layer driven- to a fully developed flow.

5 Overall Conclusions

The conclusions of greatest relevance are presented in each chapter and are once again listed below.

- DSF cavity widths affect mass flow rates in the experimental salt-water model.
- In cases where the spill plume is highly momentum-driven, cavity width does not affect horizontal velocities directly at the spill edge.
- The introduction of spandrels and their increase in height reduces horizontal spill plume velocities.
- Spandrel height has a larger influence on $\dot{m}_{f,o}$ than cavity width.
- Fully developed character of the cavity flow generally establishes earlier with increasing spandrel height.
- The presence of spandrels but also their dimensions affect the cavity flow
- Velocities along the inner plate rise with the introduction of spandrels and peak closer towards them with increasing height due to a reduction of horizontal momentum in a progressively pressure driven flow.
- Cavities affect the flow by its width dictating whether fully developed- or boundary layer–governed character prevails
- DSFs and changes in cavity width directly influence the incident heat flux on the inner and outer façade.
- A wider DSF reduces the peak HF impact along with lowering its vertical location when compared to the single skin setup.
- A narrower cavity of 0.15 m width drastically increased the total HF on the inner and outer skin when compared to the wider cavity of 0.40 m and the single façade.
- In narrow cavities the hot gas flow develops early into one well-mixed cavity flow.
- In wider cavities HF impact to inner and outer pane differs in magnitude and distribution.

- It can be inferred that there is a critical cavity width at which the cavity flow transitions from a boundary layer driven- to a fully developed flow.

The study at hand establishes the behaviour of the immediate Double-Skin Façade cavity spill flow through small-scale salt-water experiments and large scale fire tests. It has been shown that the façade geometry has a large effect on the fire flow which justifies the need for further research to be conducted. The flow interactions and various parameters influencing it, need to be investigated thoroughly to ensure well informed decision making in the fire safety engineering community is possible.

6 Bibliography

[1] Harris Poirazis, "Double Skin Facades, A Literature Review," Department of Architecture and Built Environment , Lund University, Lund Institute of Technology, Lund, 2006.

[2] Belgian Building Research Institute BBRI, "Source book for a better understanding of conceptual and operational aspects of active facades.," Department of Building Physics , Indoor Climate and Building Services, Belgian Building Research Institute, 2002.

[3] X. Loncour, A. Deneyer, M. Blasco, G. Flamant, and P. Wouters, "Ventilated Double Facades - Classification & Illustration of Facade Concepts," Department of Building Physics, Indoor Climate & Building Services, Belgian Building Research Institute, 2004.

[4] Anonymous. DeviantArt. [Online]. http://wi11iams11.deviantart.com/art/Double-glass-facade-system-321277149

[5] Jeffrey Vaglio and Mic Patterson, "Seeing Double," *US Glass Magazine*, vol. 46, no. 2, pp. 12-19, March 2011.

[6] Ajla Aksamija and Bruce Toman, "Complex Curtain Wall - Geometry and Material Selection for Passive Fire Protection," *Fire Protection Engineering*, no. 52, 2011.

[7] Adam Cowlard, Adam Bittern, Cecilia Abecassis-Empis, and Jose Torero, "Fire safety design for tall buildings," *Procedia Engineering*, no. 62, pp. 169-181, 2013.

[8] Anonymous. www.winscopenigerialtd.com. [Online]. http://www.winscopenigerialtd.com/images/B_0408_FireProtection2.gif

[9] Ni Zhaopeng, Lu Shichang, and Peng Lei, "Experimental Study on Fire Performance of Double-Skin Facades," *Journal of Fire Sciences*, September 2012.

[10] W.K. Chow, W.Y. Hung, G.W. Zou, H. Dong, and Y. Gao, "Preliminary Experimental Study of Double-Skinned Facade.," *Int. Journal on Engineering Performance-Based Fire Codes*, vol. 6, no. 3, pp. 155-167, 2004.

[11] W.K. Chow and W.Y. Hung, "Effect of cavity depth on smoke spreading of double-skin facade ," *Building and Environment*, no. 41, pp. 970-979, January 2006.

[12] LI Junmei et al., "Numerical studies on effects of cavity width on smoke spread in double- skin facade," *Procedia Engineering*, no. 45, pp. 695-699, 2012.

[13] Nadia C.L. Chow, S.S. Li, and D.X. Huang, "Apron design for protecting double-skin façade fires," *Fire and Materials*, no. 39, pp. 189-206, February 2015.

[14] E.E. Zukoski, "Properties of Fire Plumes-Chapter 3," in *Combustion Fundamentals of Fire*. UK: Elsevier Science & Technology , 1995.

[15] C.L. Chow, "Full-scale burning tests on double-skin façade fires ," *Fire and Materials*, no. 37, pp. 17-34, 2013.

[16] D. Drysdale, *An Introduction to Fire Dynamics*, Third Edition ed. UK: John Wiley & Sons, Ltd, 2011.

[17] K. Kawagoe, "Fire behaviour in rooms," Building Research Institute. Report No. 27, Tokyo, 1958.

[18] P.H. Thomas, D.L. Simms, and M. Law, "The rate of burning of wood. Fire Research Note No. 657," 1967.

[19] P.H. Thomas and A.J.M. Heselden, "Fully developed fires in single compartments. A cooperative research programme of the Conseil Internationale du Batiment. Report No. 20, Fire Research Note No. 923. ," Conseil Internationale du Batiment , 1972.

[20] D. Gross and A.F. Robertson, "Experimental fires in enclosures ," *Proceedings*

of the Combustion Institute , no. 10, pp. 931-942, 1965.

[21] P.H. Thomas, A.J.M. Heselden, and M. Law, "Fully-developed Compartment Fires: Two Kinds of Behaviour. Fire Research Technical Paper No. 18," HMSO, London, 1967.

[22] G.H. Yeoh and K.K. Yuen, *Computational Fluid Dynamics in Fire Engineering*.: Butterworth-Heinemann, 2009.

[23] A.H. Majdalani, "Compartment Fire Analysis for Contemporary Architecture," University of Edinburgh, Edinburgh, PhD Thesis 2014.

[24] J. Prahl and H. W. Emmons, "Fire-induced Flow Through an Opening," *Combustion and Flame*, vol. 25, pp. 369-385, May 1975.

[25] J. Q. Quintiere, *Principles of Fire Behaviour*. USA: Delmar Publishers, 1997.

[26] Roger Harrison and Michael Spearpoint, "Physical scale modelling of adhered spill plume entrainment," *Fire Safety Journal*, vol. 45, no. 3, pp. 149-158, 2010.

[27] S. Yokoi, "Study on the prevention of fire spread by hot upward current," Building Research Institute Report 34, 1960.

[28] John H. Klote, "Considerations of Stack Effect in Building Fires," Centre for Fire Research, U.S. Department of Commerce, National Institute of Standards and Technology , Gaithersburg, 1989.

[29] Frank M. White, *Fluid Mechanics*, 7th ed. US: Mc Graw Hill, 2011.

[30] Jamil Zinoubi, Adel Gammoudi, Taoufik Naffouti, Rejeb Ben Maad, and Ali Belghith, "Development of an Axisymmetric Thermal Plume between Vertical Plates," *American Journal of Applied Sciences*, vol. 4, no. 9, 2007.

[31] T. Naffouti, J. Zinoubi, and R. B. Maad, "Experimental Investigation of the Effect of Spacing between Vertical Plates on the Development of a Thermal Plume from an Active Block," *Journal of Applied Fluid Mechanics*, vol. 8, no. 1, pp. pp 75-84, 2015.

[32] R. Sangras and G.M. Faeth, "Buoyant Turbulent Jets and Plumes: III. Round Turbulent Nonbuoyant Starting Jets and Puffs and Buoyant Starting Plumes and Thermals," National Institute of Standards and Technology, U.S. Department of Commerce , Washington D.C., Annual Report 1999.

[33] K.D. Steckler, H.R. Baum, and J.Q. Quintiere, "Salt Water Modeling of Fire Induced Flows in Multicompartment Enclosures," in *Twenty-first Symposium (International on Combustions)*, 1986, pp. 143-149.

[34] J.M. Clement and C.M. Fleischmann, "Experimental Verification of the Fire Dynamics Simulator Hydrodynamic Model," in *Proceedings of the Seventh International Symposium*, 2002, pp. 839-851.

[35] S.P. Jankiewicz, Prediction Smoke Detector Response Using A Quantitative Salt-water Modeling Technique, 2004.

[36] Xiaobo Yao, Characterization of Fire Induced Flow Transport along Ceilings using Salt-Water Modeling , 2006.

[37] Chan Chau Siang, Characterizing Smoke Dispersion along Beamed Ceilings using Salt-Water Modeling, 2010.

[38] J. G. Quintiere, "Scaling Applications in Fire Research," *Fire Safety Journal*, vol. 15, pp. 3-29, 1989.

[39] G. Heskestad, "Physical Modeling of Fire ," *Fire and Flammability*, vol. 6, pp. 253-273, 1975.

[40] F. A. Williams, "Scaling Mass Fires," *Fire Research Abstracts and Reviews*, vol. 11, pp. 1-22, 1969.

[41] Thomas George Layton, "Detailed Measurements of Fire-Induced Mixing Phenomena," College Park, Maryland, MSc Thesis 2014.

[42] A. A. Kelly, "Examination of Smoke Movement in a Two-Story Compartment Using Salt-Water and Computational Fluid Dynamics Modeling," Fire

Protection Engineering, University of Maryland, College Park, MSc Thesis 2001.

[43] C. S. Chan, "Characterizing Smoke Dispersion Along Beamed Ceilings UsingSalt-Water Modeling," Fire Protection Engineering, University of Maryland, College Park, MSc Thesis 2010.

[44] Markus Raffel, Christian E. Willert, and Jürgen Kompenhans, *Particle Image Velocimetry: A Practical Guide*. Berlin, Germany: Springer Science & Business Media, 1998.

[45] R. D. Keane and R. J. Adrian, "Optimization of particle image velocimeters. I. Double pulsed Systems," *Measurement Science and Technology*, vol. 1, no. 11, p. 1202, 1990.

[46] Incropera, F.P.; et al, "Fundamentals of Heat and Mass Transfer, 6th Edition," Hoboken, NJ, 2007.

[47] Yogesh Jaluria, "Natural Convection: Heat and Mass Transfer (HMT--The Science & Applications of Heat and Mass Transfer) ," 1980.

[48] Hidalgo, J.P.; Cowlard, A.; Abecassis-Empis, C.; Maluk, C.; Majdalani, A.H.; Kahrmann, S.; Hilditch, R.; Krajcovic, M.; Torero, J.L.;, "Edinburgh Tall Building Fire Tests – Part 1: Experimental Series and Setup Description (submitted)," *Fire Safety Journal*, 2015.

[49] J.P. Hidalgo, "Performance-Based Methodology for the Fire Safe Design of Insulation Materials in Energy Efficient Buildings," University of Edinburgh, Edinburgh, PhD Thesis 2015.